A drag coefficient model for Lagrangian particle dynamics relevant to high-speed flows

Raghava S. C. Davuluri, Sean C. C. Bailey, Kaveh A. Tagavi, Alexandre Martin*

Mechanical Engineering, University of Kentucky, Lexington, KY, 40506, USA

Abstract

A blended drag coefficient model is constructed using a series of empirical relations based on Reynolds number, Mach number, and Knudsen number. When validated against experiments, the drag coefficient model produces matching values with a standard deviation error of 2.84% and a maximum error of 11.87%. The model is used in a Lagrangian code which is coupled to a hypersonic aerothermodynamic CFD code, and the particle velocity and trajectory are validated against experimental results. The comparative results agree well and show that the new blended drag coefficient model is capable of predicting the particle motion accurately over a range of Reynolds number, Mach number, and Knudsen number.

Keywords: Lagrangian Particle Trajectory, Particle-laden flows, Drag coefficient, Hypersonics, Aerothermodynamics

Nomenclature

Symbols

a	Speed of sound, m/s
A	Area of cross-section, m^2
C	Compressibility factor
C_D	Drag coefficient
d	Diameter, m
E	Internal energy, J/kg
F	Force, N
$\mathbf{F}$	Force vector, N
$\boldsymbol{\mathcal{F}_c}$	Convective flux matrix
$\boldsymbol{\mathcal{F}_d}$	Diffusive flux matrix

*Corresponding author

Email addresses: raghava.davuluri@uky.edu (Raghava S. C. Davuluri), sean.bailey@uky.edu (Sean C. C. Bailey), kaveh.tagavi@uky.edu (Kaveh A. Tagavi), alexandre.martin@uky.edu (Alexandre Martin)

k	Slip coefficient
Kn	Knudsen number
L	Characteristic length, m
M	Mach number
$\dot{m}$	Rate of change of mass due to chemical reactions, kg/s
m	Mass, kg
p_{force}	Power required to overcome force, W
$\dot{q}$	Heat rate, W
$\mathbf{Q}$	Conservative variables vector
r	Radius, m
Re	Reynolds number
S	Molecular speed ratio ($= M\sqrt{\frac{\gamma}{2}}$)
$\dot{\mathbf{S}}$	Source term vector for KATS
T	Temperature, K
(u, v, w)	Velocity components in axial, radial and z-directions, m/s
$\mathbf{U}$	State vector
$\mathbf{V}$	Velocity vector, m/s
$\mathbf{W}$	Source vector
Y_i	Mass fraction, kg/kg
(x, y, z)	Position components in axial, radial and z-directions, m
γ	Ratio of specific heats
ϵ	Error
ϵ'	Correction term for k
λ	Molecular mean free path, m
ρ	Density, kg/m^3
ζ	Rarefaction parameter

Subscripts

conv	Convection
exp	Experimental
f	Surrounding fluid
num	Numerical
p	Particle
r	Relative

rad	Radiation
rxn	Chemical reactions
u	Uncertainty
w	Wall
∞	Free-stream

1. Introduction

Particle-laden flows are an essential class of multiphase flows in which small, discrete particles are immersed within a carrier fluid. Several notable examples can be found in nature or technology (e.g., rocket nozzle flows [1, 2]; resuspension phenomena [3]; dusty-laden environmental flows [4, 5]; sprays [6]; granular flows [7]; powder flows [8]; and slurry flows [9]). Seeding particles are also intentionally introduced into fluids to enable measurement of the fluid velocity (e.g., Particle Image Velocimetry - PIV [10, 11]; Particle Tracking Velocimetry - PTV [12]; and Laser Doppler Anemometry - LDA [13, 14]).

The primary approaches used to model particle-laden flows are Eulerian-Eulerian, Eulerian-Lagrangian, and fully Eulerian with fluid-structure interaction (FSI) methods. In the Eulerian-Eulerian method, the carrier fluid, as well as discrete particles, is treated as continuous and interpenetrating continua. Both the particle phase and the carrier fluid phase are solved using the Navier-Stokes equations. The set of equations for the two-phase flow is solved in the Eulerian frame of reference, and the method is primarily used when the volume fraction of the particles is high. In this methodology, various bins of particles, each with a specific size, are assumed, and additional relationships are used to account for particle-wall and particle-particle interactions.

A fully Eulerian with FSI method is used in the cases where discrete particles undergo large structural deformation and phase change in carrier fluid flow. There are various approaches to model the particle flows using this methodology [15, 16, 17, 18]. Based on the approach, carrier fluid employs Eulerian or arbitrary Lagrangian-Eulerian formulations, whereas Lagrangian formulation is used for discrete particles. This method can be used for particles that vary in size.

In the case of the Eulerian-Lagrangian method, the carrier fluid is treated as a continuum, and governing Navier-Stokes equations are solved in the Eulerian frame of reference. The interactions of the discrete particles with the carrier fluid are then modeled in the Lagrangian frame of reference, *a posteriori* using information from the solution for the carrier fluid. The method can be employed for particles that vary in size when interactions between the two phases are essential to consider.

The particles interact with the carrier fluid through mass, momentum, and energy. The mass interaction between the particles and the fluid takes place in the form of chemical reactions. The chemical products from the reactions change the composition of the fluid and size (and shape) of the particles. On the other hand, the momentum interactions take place in the form of force exerted by the fluid and reaction force from the particles. The fluid dictates the motion of the particle through the exertion of forces. The various types of forces exerted on the particle by the fluid are discussed in Section 2.3 briefly. The reaction force from the discrete particles may change the velocity of the fluid. Lastly, the work done by the exerted forces and the heat transfer between the fluid and particle constitutes the energy interactions. The energy interactions results in a change in the temperature of discrete particles and the carrier fluid.

Accurately modeling particle behavior can be essential in the study of the thermal protection system (TPS) behavior during atmospheric entry. The fibrous ablative materials that are used as a TPS in many space vehicles counter the high heat rates and have been observed to expel particles in a process referred to as "spallation" [19, 20, 21, 22, 23, 24]. Experiments have found that this phenomenon is a non-negligible mechanism of surface degradation [25], and particles shed from the surface could introduce additional chemical species outside of the surface boundary layer [26]. Modeling the particle trajectories in these types of flows, however, is complicated by the potential for individual particles to experience flow regimes ranging from subsonic to hypersonic, within gases which can be rarefied or continuum.

Here, we present and validate a Lagrangian particle trajectory prediction and interaction model implemented within a computational fluid dynamics framework following the Euler-Lagrangian method. To facilitate the use of this model in the study of the spallation of TPS materials [27], the model was designed to predict particle trajectories for the full range of subsonic to hypersonic flow regimes and a wide range of Knudsen numbers. The objective of this study is to demonstrate that the numerical model can predict the particle motion. The objective is achieved in two steps. First, a blended drag coefficient model is constructed using a series of empirical relations based on the flow and particle conditions. Validation is performed by comparing the results of the model with experiments, ensuring that the model is valid over various regimes. Then, the model is used in a Lagrangian particle code and coupled to a hypersonic aerothermodynamic CFD code so that particle properties (velocity and trajectory) can be validated against experimental results.

2. Numerical Approach

2.1. Particle motion

The particle model simulates the dynamics of a particle by employing a Lagrangian formulation [28] and includes the chemical interaction of the particle with the flow field [27]. The model assumes the particle to be spherical in shape. In order to build the model, the governing equations are cast in the form of

$$\frac{\partial \mathbf{U}}{\partial t} = \mathbf{W} \tag{1}$$

where $\mathbf{U}$ is the state vector, and $\mathbf{W}$ is the source term vector. The elements of the vectors are then represented as

$$\mathbf{U} = \begin{pmatrix} m_p \\ m_p u_p \\ m_p v_p \\ m_p w_p \\ m_p E_p \end{pmatrix}, \qquad \mathbf{W} = \begin{pmatrix} \dot{m}_{\text{chemistry}} \\ F_{p_x} \\ F_{p_y} \\ F_{p_z} \\ \dot{q}_{\text{conv}} + p_{\text{force}} - \dot{q}_{\text{rad}} + \dot{q}_{\text{rxn}} \end{pmatrix} \tag{2}$$

where m_p is the mass of the particle, with (u_p, v_p, w_p) its Cartesian velocity components, and E_p its total energy. The particle mass can be altered through the chemical reaction source term $\dot{m}_{\text{chemistry}}$; the velocity through the Cartesian components of total force acting on the particle $\left(F_{p_x}, F_{p_y}, F_{p_z}\right)$; and the total energy through the convective ($\dot{q}_{\text{conv}}$), radiative ($\dot{q}_{rad}$), and reaction ($\dot{q}_{\text{rxn}}$) heat rates, as well as through the power required to overcome force acting on the particle (p_{force}). The chemistry model accounts for oxidation, nitridation, and sublimation of carbon particle. Though the chemistry model was previously used on carbon particles, similar models can be employed for particles of other compositions. The discretization of the system of equations in Eq. 2 is performed using the backward Euler method. The mass conservation equation is uncoupled from momentum and energy conservation equations, and the block Gauss-Seidel method is used to solve the two sets of equations. The set of momentum and energy equations are solved using Newton's method. This approach has been verified using the method of manufactured solution [29], which confirmed the order of accuracy of the discretization and correctness of the numerical code.

2.2. Flow field

The flow fields used in this study are determined using converged solutions of the aerothermodynamic computational fluid dynamics (CFD) code KATS. KATS is a laminar aerothermodynamics Navier-Stokes solver that uses a finite-volume approach with various modules [30, 31, 32, 33] for simulating complex phenomena in ablation-related problems, including spallation studies [27, 28, 26, 24]. The module KATS-CFD is used for computing compressible viscous flows including thermo-chemical nonequilibrium flows by solving the corresponding governing equations in the form

$$\frac{\partial \mathbf{Q}}{\partial t} + \nabla \cdot (\boldsymbol{\mathcal{F}_c} - \boldsymbol{\mathcal{F}_d}) = \dot{\mathbf{S}} \quad , \tag{3}$$

where $\mathbf{Q}$ is a vector of conservative variables, $\boldsymbol{\mathcal{F}_c}$ and $\boldsymbol{\mathcal{F}_d}$ are convective and diffusive flux matrices, and $\dot{\mathbf{S}}$ is a source term vector. For solution, the system of equations represented in Eq. 3 is discretized first-order in time and second-order in space. The solver uses the PETSc library [34, 35, 36] to solve the linear system of equations, with ParMETIS [37] used for domain decomposition, and MPI [38] for message passing. More information regarding the solver is given in Ref. [39]. The coupling of the Lagrangian particle code and the hypersonic aerothermodynamic CFD code was developed in previous works, and used to study the effects of the flow field on the particles, and vice-versa [26, 27, 28].

2.3. Drag coefficient

To obtain $\mathbf{F_p} = (F_{p_x}, F_{p_y}, F_{p_z})$, we note that the rate of change of momentum of a particle can be described by the Basset-Boussinesq-Oseen (BBO) equation [40] which defines

$$\mathbf{F_p} = \mathbf{F_p}_{\text{drag}} + \mathbf{F_p}_{\text{pressure}} + \mathbf{F_p}_{\text{add}} + \mathbf{F_p}_{\text{bassett}} + \mathbf{F}_{\text{ext}} \quad , \tag{4}$$

where $\mathbf{F_p}_{\text{drag}}$ is the steady-state drag force acting on the particle that assumes no change of relative velocity between the particle and carrier fluid, and a uniform pressure field. $\mathbf{F_p}_{\text{drag}}$ is equal to the sum of pressure and shear forces acting on the particle surface. $\mathbf{F_p}_{\text{pressure}}$ is the force due to the local pressure gradient that accelerates the particle – also referred to as the buoyancy force – and is equivalent to the weight of the fluid displaced that would otherwise occupy the volume of the particle. This force plays a significant role in slurry flows and bubbly flows [40]. $\mathbf{F_p}_{\text{add}}$ is an unsteady force term called *the added mass force*. When a particle accelerates, it displaces fluid around it. Therefore, the force acting on the particle depends on an effective mass, which is equivalent to the sum of particle mass and added mass that comes from the change in inertia in the fluid. For spheres, the added mass is equal to half of the mass of the fluid displaced by the particle [41]. $\mathbf{F_p}_{\text{bassett}}$ is also an unsteady force term and is called Basset force or Basset history force. While $\mathbf{F_p}_{\text{add}}$ accounts for pressure effects on the particle due to acceleration, $\mathbf{F_p}_{\text{bassett}}$ accounts for viscous effects [40]. When the particle accelerates through the fluid, there is a change in its relative velocity with respect to time. The change in relative velocity causes the boundary layers around the particle to change. However, it takes some time for the boundary layers to respond to the change, and $\mathbf{F_p}_{\text{bassett}}$ accounts for this temporal delay. Lastly, $\mathbf{F}_{\text{ext}}$ denotes external forces such as gravity.

The drag force $\mathbf{F_p}_{\text{drag}}$ is a function of fluid and particle velocities, and is included in Eq. 4 for all conditions. The added mass force $\mathbf{F_p}_{\text{add}}$ is present when a relative acceleration is detected between the phases. This term becomes more significant when there is an increase in volume fraction and particle size [42]. The Basset force $\mathbf{F_p}_{\text{bassett}}$ only plays an important role in unsteady flows. This force increases when the volume fraction, particle size, fluid density, or fluid viscosity increases [42, 43]. The magnitudes of $\mathbf{F_p}_{\text{add}}$ and $\mathbf{F_p}_{\text{bassett}}$ are directly dependent on ratio of fluid to particle density [44].

Several studies were performed [45, 46, 47, 48], which determined that for smaller particles (order of size: 0.1-100 μm) and high flow velocities, all but the drag force were insignificant. The drag force acting on the particle can be expressed as

$$\mathbf{F_p}_{\text{drag}} = \frac{1}{2} C_D \rho_f A_p |\mathbf{V_r}| \mathbf{V_r} \tag{5}$$

so that the direction of $\mathbf{F_p}_{\text{drag}}$ is inverse to that of $\mathbf{V_r}$, the relative velocity of the particle to the surrounding fluid, and is defined as $(\mathbf{V_p} - \mathbf{V_f})$, where $\mathbf{V_p}$ represents the particle velocity vector and $\mathbf{V_f}$ is the velocity vector of the surrounding fluid. The drag coefficient, as used in the above equation, includes all the physical mechanisms that are responsible for the interphase force between the particles and the fluid, including pressure, viscous, and wave drags. The drag coefficient is also a function of the shape of the body. However, the model and the following discussion pertains only to spherical particles. The drag coefficient depends on various fluid flow conditions, which can be summed up its dependence on three dimensionless parameters: Reynolds number (Re), Mach number (M), and Knudsen number (Kn).

Reynolds number is defined as the ratio of inertial to viscous forces. In the case of spheres, it is defined as:

$$\mathrm{Re} = \frac{\text{Inertial forces}}{\text{Viscous forces}} = \frac{\rho_f |\mathbf{V_r}| d_p}{\mu_f} \tag{6}$$

where ρ_f is the density of the fluid flowing over the sphere, d_p is the diameter of the sphere, and μ_f is the dynamic viscosity of the fluid. For low Reynolds number ($\mathrm{Re} < 1$) where viscous forces are dominant and inertial forces are negligible, C_D is inversely proportional to Re and is within what is referred to as *Stoke's regime* [49, 44]. In this regime – in the context of continuum – the flow remains attached to the particle with no wake formation. As the Reynolds number increases ($1 < \mathrm{Re} < 1000$), the inertial forces become effective with flow separation, wake formation, and vortex shredding taking place. This regime is referred to as the *intermediate regime*, and the inverse relationship between C_D and Re continues until the former reaches a constant value. In this regime, the sum of form drag and viscous drag contribute to C_D. With the further increase in Re, the inertial forces become dominant over viscous forces. As Re increases beyond 1000, the wake region becomes turbulent, whereas the boundary layer region in front remains laminar. This flow regime is called *Newton's regime*, where C_D is only due to form drag and remains relatively constant until the critical Re is reached. At the critical Re ($\sim 3 \times 10^5$), both the boundary layer and wake region become turbulent. The separation point is further moved rearward, which causes a sharp decline in form drag and, thus, a sudden decrease in C_D. Following the decline, C_D increases with the increase in Re. The dependency of C_D on Re, as described above, indicate the *inertial/viscous effects*. The surface roughness, which also affects the drag coefficient, is not considered in this work, and the particles are assumed to be smooth.

Mach number is defined as the ratio between the relative velocity of the body and speed of sound and is defined as:

$$\mathrm{M} = \frac{|\mathbf{V_r}|}{a_f} \tag{7}$$

where a_f is the speed of sound of the fluid through which the body travels. The Mach number dependency denotes the *compressibility effects* on the drag coefficient. It should be noted that the behavior of C_D with respect to Re, as explained above, is for incompressible and continuum flow. With compressibility included, C_D does not follow the same trend as described above. However, simplifications assumed in describing the behavior of C_D are often justified. For low Mach numbers (M $<$ 0.5), C_D is relatively independent of M [40]. With the increase in M, C_D increases until the flow reaches the sonic condition (M $=$ 1) where there is a significant jump caused by the formation of the shock wave in front of the body. The presence of shock wave produces a sudden rise in the forebody and afterbody pressure distribution that affects the drag force. However, this change in the C_D value is entirely dependent on Re. The transition is smooth for higher Reynolds number flows (Re $> 10^5$), non-smooth for moderate Reynolds number flows ($200 <$ Re $< 10^4$), and accompanied by significant changes to a small change in M for low Reynolds number flows (Re $<$ 200) [50, 51, 52, 53, 54]. With an increase in Mach number above 1, there is a rapid increase in C_D until it reaches a point where the increase is relatively small. In these high Mach number regimes, C_D has a stronger dependence on M, followed by Re. Also, for low Reynolds number flows, C_D is seen to decrease with an increase in Mach number without reaching a maximum value near M $=$ 1 [40]. This behavior is caused by the rarefied condition, which will be discussed below.

The nature of $\mathbf{F}_{\mathbf{p}_{\mathrm{drag}}}$ is highly dependent on the size of the particle relative to the intermolecular spacing of the carrier fluid. Hence, to characterize this ratio, we employ the Knudsen number, defined as the ratio of the molecular mean free path, λ, and characteristic length, L [55]. The Knudsen number is defined as

$$\mathrm{Kn} = \frac{\lambda}{L} = \begin{cases} \frac{\mathrm{M}}{\mathrm{Re}}\sqrt{\frac{\pi\gamma}{2}}, & \text{if } \mathrm{Re} \leq 1, \\ \mathrm{M}\sqrt{\frac{\pi\gamma}{2\mathrm{Re}}}, & \text{if } \mathrm{Re} > 1. \end{cases} \tag{8}$$

The characteristic length, L, corresponds to the length scale through which the carrier fluid interacts with the particle. The characteristic length is approximately equal to the boundary layer thickness (δ) for the flows where Re is higher than one and is equivalent to the particle diameter(d_p) for highly rarefied flows or for the flows where Re is less than or equal to 1 [56].

It should be noted that some studies used particle diameter and some used particle radius as characteristic length in defining Kn [55]. However, the study conducted by Macrossan [57] indicated that Eq. 8 is a more valid definition of Kn.

As Kn increases, the molecular interactions at the surface of the particle can change with different regimes of interaction defined based on the Knudsen number: continuum flow (Kn ≤ 0.01); slip flow ($0.01 <$ Kn ≤ 0.1); transition flow ($0.1 <$ Kn ≤ 10); and free-molecular flow (Kn ≥ 10). In the continuum and slip flow regimes, $\mathbf{F}_{\mathbf{p}_{\mathrm{drag}}}$ is caused by both pressure and viscous forces. However, the compressibility of the flow modifies the pressure distribution into forebody and afterbody. For subsonic, incompressible flows, C_D loosely follows the "standard curve" [51] where its only dependence is on Re. However, as M increases, the compressibility effects become increasingly important and must be taken into account.

Within transition and free molecular flow regimes, the continuum concepts of pressure and viscosity lose meaning. $\mathbf{F}_{\mathbf{p}_{\mathrm{drag}}}$ is better described as the difference between the momentum imparted by the incoming molecules and momentum imparted by molecules that recoil from the body [58]. Within compressible flow behind a normal shock wave [59, 60, 61], it has been observed that C_D depends on the wall temperature of the particle and Re. As the Kn increases from transition to free-molecular regimes, $\mathbf{F}_{\mathbf{p}_{\rm drag}}$ becomes increasingly dependent on these parameters.

At low Mach numbers (M << 1), C_D decreases as Kn increases. In the slip and transition regimes, the C_D value increases as Kn increases and M decreases (for large Mach numbers). In the free-molecular regime, C_D is more dependent on the molecular speed ratio and the surface temperature of the particle since the drag no longer depends on the viscosity of the fluid [40, 54]. The molecular speed ratio is defined as the ratio of relative velocity of the body and "most probable" thermal velocity of the gas molecules [62]. The values of C_D increases with molecular speed ratio until it reaches a value of unity (high transonic flows), and then decreases, approaching 2 as molecular speed ratio approaches infinity [63]. Similarly, C_D increases as the ratio of the surface temperature of the particle to surrounding fluid temperature increases [54, 61]. The above-described behavior is usually referred as *rarefaction effects* on the drag coefficient.

In the incompressible and continuum regime, the behavior of C_D is dominated by inertial/viscous effects. The compressible effects dictate the C_D behavior for flows with higher Reynolds number (Re $> 45-60$), whereas rarefaction effects dictate the behavior for flows with low Reynolds number (Re $< 45-60$) [50, 54, 64]. It can be inferred from Eq. 8 that the Kn regimes can be due to lower Re and/or higher M. Therefore, rarefaction effects occur along with inertial/viscous or compressible effects, and vice-versa. The regions where such a combination of effects occur are the compressible regime with low to moderate Re, and the incompressible regime with low Re.

Numerous empirical models for C_D have been proposed which cover the range of Re, M, and Kn, and these models are summarized in Table 1. The formulations of these empirical models correspond to the drag coefficient of spherical particles. In this table, $(\mathrm{Re_r}, \mathrm{M_r}, \mathrm{S_r})$ and $(\mathrm{Re}_\infty, \mathrm{M}_\infty, \mathrm{S}_\infty)$ indicate the Reynolds number, Mach number, and molecular speed ratio based on relative velocity and free-stream conditions, respectively. The ratio of wall temperature (in this case, the temperature of the particle, assuming it is isothermal) to the free-stream temperature of the gas is represented by $\left(\frac{T_w}{T_\infty}\right)$. More specifically, these are defined as

$$\mathrm{Re_r} = \frac{\rho_f |\mathbf{V}_\mathrm{r}| d_p}{\mu_f}, \quad \mathrm{M_r} = \frac{|\mathbf{V}_\mathrm{r}|}{a_f}, \quad \text{and} \quad \mathrm{S_r} = \mathrm{M_r}\sqrt{\frac{\gamma}{2}} \tag{9}$$

$$\mathrm{Re}_\infty = \frac{\rho_\infty |\mathbf{V}_\infty| d_p}{\mu_\infty}, \quad \mathrm{M}_\infty = \frac{|\mathbf{V}_\infty|}{a_\infty}, \quad \text{and} \quad \mathrm{S}_\infty = \mathrm{M}_\infty\sqrt{\frac{\gamma}{2}} \tag{10}$$

where ρ, μ, a, γ are the density, dynamic viscosity, speed of sound, ratio of specific heats of the carrier fluid, and d_p the diameter (or size) of the particle. The subscript "f" indicates the properties of fluid surrounding the particle, whereas "∞" represents the properties of the fluid in the free-stream region.

Stokes developed an expression for C_D through the solution of the incompressible Navier-Stokes equation for the condition where Re << 1. Oseen [65] included some convective effects and produced an expression with extended validity (Re $<$ 5). The Reynolds number range was further extended by Schiller and Nauman [66, 67] to Re $<$ 200 by empirically using experimental data with a similar expression also developed by Walsh [68]. These formulations, being based on Stokes initial solution of the incompressible Navier-Stokes equation, implicitly assume continuum flow at low M.

Cunningham [69] assumed a constant slip velocity of the fluid, due to rarefaction, on the surface of the sphere, which is equal to $(1-k)\,\mathbf{V_r}$ where k is the slip coefficient. Cunningham derived the relation between the Kn and k which is expressed as

$$k = \left(1 + \frac{9}{2}\mathrm{Kn}\right)^{-1} \tag{11}$$

As his model is a modification of the Stokes solution, it is valid for Re $<<$ 1 and M $<$ 0.3, but only valid for Kn $\leq$ 0.1.

Carlson and Hoglund [71] developed a drag model by adding correction terms for continuum and free-molecular regimes. The term for rarefaction effect was added from Millikan's model [73] with the constants determined from the experiment [74]. The inertial effect term was the same as Schiller and Nauman's model [66], and the compressibility term was taken from Hoerner's model [62]. The model works well for M $\leq$ 2 and 0.1 $\leq$ Re $\leq$ 100.

Henderson's [72] C_D model was constructed using two sets of equations, one for M $<$ 1 and one for M $>$ 1.75, with linear interpolation, applied to obtain C_D in the range 1 $\geq$ M $\leq$ 1.75. For M $<$ 1, the Oseen model [65] was used for the continuum regime, Millikan's model [73] for the slip and transition regimes, and an exponential correction term added to account for compressibility effects. For the free molecular regime, the Langevin [75] and Epstein [76] models were used. Similarly, for M $>$ 1.75, an empirical relationship as a function of Re_∞, M_∞, and S_∞ was developed using the experimental data of Refs. [61, 74]. This model works well for continuum, slip, transition, and free-molecular flow for M $<$ 6 and Re up to the laminar-turbulence transition $\left(\sim 3 \times 10^5\right)$. It should be noted that all the empirical models listed in Table 1 are functions of $\mathrm{Re_r}$, $\mathrm{S_r}$, and $\mathrm{M_r}$ (based on the relative velocity of the particle). However, the Henderson C_D model uses $\mathrm{Re_r}, \mathrm{S_r}, \mathrm{M_r}$ for flows with M $<$ 1, but uses $\mathrm{Re}_\infty, \mathrm{S}_\infty, \mathrm{M}_\infty$ for flows with M $>$ 1.75. The model also includes the effect of the particle's temperature on the drag coefficient through the variable (T_w/T_∞).

Tedeschi [70] developed an empirical relationship by using the same methodology as Cunningham [69] but for an extended Re range, and applied it on the Schiller and Nauman [66] formulation. Furthermore, to include compressibility effects, parameter C was added. Rarefaction effects were introduced through a rarefaction parameter ζ and a slip coefficient k. The empirical relationships for the parameters were

Table 1: Previously proposed drag-coefficient formulations for particles

Model	Formulation	
Stokes	$C_D = \dfrac{24}{\mathrm{Re_r}}$	(12)
Oseen [65]	$C_D = \dfrac{24}{\mathrm{Re_r}}\left(1 + \dfrac{3}{16}\mathrm{Re_r}\right)$	(13)
Schiller and Nauman [66]	$C_D = \dfrac{24}{\mathrm{Re_r}}\left(1 + 0.15\mathrm{Re_r}^{0.687}\right)$	(14)
Cunningham [69]	$C_D = \dfrac{24}{\mathrm{Re_r}}\left(1 + \dfrac{9}{2}\mathrm{Kn}\right)^{-1}$	(15)
Tedeschi [70]	$C_D = \dfrac{24}{\mathrm{Re_r}}k\left[1 + 0.15\left(k\mathrm{Re_r}\right)^{0.687}\right]\zeta(\mathrm{Kn})C$	(16)
Carlson and Hoglund [71]	$C_D = \dfrac{24}{\mathrm{Re_r}}\dfrac{\left[1+0.15\mathrm{Re_r}^{0.687}\right]\left[1+\exp\left(-\frac{0.427}{\mathrm{M_r}^{4.63}} - \frac{3}{\mathrm{M_r}^{0.88}}\right)\right]}{1+\frac{\mathrm{M_r}}{\mathrm{Re_r}}\left[3.82 + 1.28\exp\left(-1.25\frac{\mathrm{Re_r}}{\mathrm{M_r}}\right)\right]}$	(17)
Henderson [72]	$C_D = \begin{cases} 24\left[\mathrm{Re_r} + \mathrm{S_r}\left\{4.33 + \dfrac{3.65 - 1.53\left(\frac{T_w}{T_\infty}\right)}{1+0.353\left(\frac{T_w}{T_\infty}\right)}\exp\left(-0.247\frac{\mathrm{Re_r}}{\mathrm{S_r}}\right)\right\}\right]^{-1} \\ +\exp\left(-\frac{0.5\mathrm{M_r}}{\sqrt{\mathrm{Re_r}}}\right)\left[\dfrac{4.5+0.38\left(0.03\mathrm{Re_r}+0.48\sqrt{\mathrm{Re_r}}\right)}{1+0.03\mathrm{Re_r}+0.48\sqrt{\mathrm{Re_r}}} + 0.1\mathrm{M_r}^2 + 0.2\mathrm{M_r}^8\right] \\ +0.6\mathrm{S_r}\left[1-\exp\left(-\frac{\mathrm{M_r}}{\mathrm{Re_r}}\right)\right], \ \text{if } \mathrm{M}\le 1 \\ C_{D_{(\mathrm{M}=1)}} + \frac{4}{3}\left(\mathrm{M}_\infty - 1\right)\left(C_{D_{(\mathrm{M}=1.75)}} - C_{D_{(\mathrm{M}=1)}}\right), \ \text{if } 1<\mathrm{M}\le 1.75 \\ \dfrac{0.9+\left(\frac{0.34}{\mathrm{M}_\infty^2}\right)+1.86\left(\frac{\mathrm{M}_\infty}{\mathrm{Re}_\infty}\right)^{\frac{1}{2}}\left[2+\frac{2}{\mathrm{S}_\infty^2}+\frac{1.058}{\mathrm{S}_\infty}\left(\frac{T_w}{T_\infty}\right)^{\frac{1}{2}}-\frac{1}{\mathrm{S}_\infty^4}\right]}{1+1.86\left(\frac{\mathrm{M}_\infty}{\mathrm{Re}_\infty}\right)^{\frac{1}{2}}}, \ \text{if } \mathrm{M}>1.75 \end{cases}$	(18)

developed using the experimental results of Refs. [61, 51, 77, 50]. The parameters are formulated as

$$C\left(\mathrm{Re},\mathrm{M}\right) = 1 + \frac{\mathrm{Re}_\mathrm{r}^2}{\mathrm{Re}_\mathrm{r}^2 + 100}\exp\left(\frac{-0.225}{\mathrm{M}_\mathrm{r}^{2.5}}\right) \tag{19}$$

$$\zeta\left(\mathrm{Kn}\right) = 1.177 + 0.177\frac{0.851\mathrm{Kn}^{1.16} - 1}{0.851\mathrm{Kn}^{1.16} + 1} \tag{20}$$

$$b_1 k^{1.687} + b_2 k - 1 = 0 \tag{21}$$

where the slip coefficient k is derived by solving the above non-linear equation (Eq. 21). The coefficients in the equation are defined as

$$b_1 = \frac{9}{4}\left(0.15\right)\frac{L}{r_p}\frac{\mathrm{Kn}}{\epsilon'}\left(\frac{2r_p}{L}\frac{\mathrm{S_r}\sqrt{\pi}}{\mathrm{Kn}}\right)^{0.687} \quad \text{and} \quad b_2 = 1 + \frac{9}{4}\frac{L}{r_p}\frac{\mathrm{Kn}}{\epsilon'} \tag{22}$$

where L is the characteristic length used in defining Kn, r_p is the radius of the particle, $\mathrm{S_r}$ is the molecular speed ratio based on the relative velocity of the particle, and ϵ' is the correction term applied to the slip coefficient with $\mathrm{S}' = \left(1-k\right)\mathrm{S_r}$. The ratio between the characteristic length, L, and radius of the particle, r_p, can be expressed as

$$\frac{L}{r_p} = \begin{cases} 2, & \text{if } \mathrm{Re_r} \leq 1 \\ 2/\sqrt{\mathrm{Re_r}}, & \text{if } \mathrm{Re_r} > 1 \end{cases} \tag{23}$$

and the expression for ϵ' is given as

$$\epsilon' = \frac{3}{8}\left(\frac{\sqrt{\pi}}{\mathrm{S}'}\right)\left(1 + \mathrm{S}'^2\right)\mathrm{erf}\left(\mathrm{S}'\right) + \frac{\exp\left(-\mathrm{S}'^2\right)}{4}. \tag{24}$$

The Tedeschi drag coefficient model is intended to be valid in the continuum, slip, and transition regimes. The accuracy of the Tedeschi C_D model has been demonstrated successfully for flows with $\mathrm{M} \leq 1$ and $\mathrm{Re} \leq 200$ for all Kn.

As noted, the drag coefficient for each model discussed above is given in Table 1, with each having a distinct range of valid Re, Kn, and M. The objective here is to use these models to prepare a blended C_D model that can be implemented numerically by choosing an appropriate model for a given regime. The results of this amalgamated model are then compared to experimental results for validation. The specific studies used for comparison to model predictions are presented in Table 2.

3. Blended Drag Coefficient Model Construction

The collection of experimental data [78, 79, 80, 58, 77, 61] presented in Table 2, covers a range of values $0.12 \leq \mathrm{M} \leq 6.4$, $3 \leq \mathrm{Re} \leq 50{,}000$, and $\mathrm{Kn} \leq 2$, that is, from subsonic to the hypersonic regime, from low to high Reynolds number, and from continuum to transitional flow regime. All the experiments shown in Table 2 were conducted on spherical particles. It should be noted that Aroesty's [58] experimental data for

Table 2: Drag-coefficient measurements used for comparison to model results.

Experiment	Flow conditions	Uncertainty error
Kane [78]	$2.1 < \mathrm{M}_\infty < 2.8$ $15 < \mathrm{Re}_\infty < 800$ $0.1 < \mathrm{Kn}_\infty < 1$	5%
Wegener and Ashkenas [79]	$3.8 < \mathrm{M}_\infty < 4.3$ $50 < \mathrm{Re}_\infty < 1000$ $0.006 < \mathrm{Kn}_\infty < 0.106$	10%
Sreekanth [80]	$\mathrm{M}_\infty = 2$ $3 < \mathrm{Re}_\infty < 60$ $0.1 < \mathrm{Kn}_\infty < 1$	4%
Aroesty [58]	$\mathrm{M}_\infty = 2, 4, 6$ $10 < \mathrm{Re}_\infty < 10,000$ DB - $0.001 < \mathrm{Kn}_\infty < 0.3$ MM - $0.1 < \mathrm{Kn}_\infty < 1.2$	 7%, 4%, 5% 7%, 6%, 5%
Lawrence [77]	$0.17 < \mathrm{M}_\infty < 0.99$ $185 < \mathrm{Re}_\infty < 11,600$ $0.002 < \mathrm{Kn}_\infty < 0.1$	2%
Bailey and Hiatt [61, 51]	$0.12 < \mathrm{M}_\infty < 6.39$ $15 < \mathrm{Re}_\infty < 50,300$ $0.001 < \mathrm{Kn}_\infty < 2$	2%

the sphere drag coefficient is classified into two sets: the Drag Balance (DB) and the Moving Model (MM). For the DB data, the drag was measured on mounted spheres in a wind tunnel. The MM data corresponds to experiments where drag was measured on small spheres that were freely falling through a wind tunnel jet. The MM data also consists of drag coefficient values for different T_w/T_∞ values.

Sreekanth [80], and Wegener and Ashkenas [79] provided the data in the form of a triplet $(\mathrm{M}, \mathrm{Re}, \mathrm{Kn})$ where Kn was calculated from the measurements made. Other sets of experimental data [78, 58, 77, 61] were in the form of $(\mathrm{M}, \mathrm{Re})$ doublets, and Kn was calculated using Eq. 8. In the case of the Sreekanth [80] data, Kn was calculated using the particle diameter as characteristic length for $\mathrm{Re} > 1$. This resulted in significant discrepancies between C_D and its theoretical free-molecular flow value at a low Kn. Similar disagreements, for C_D as a function of Kn, were also found for the Wegener and Ashkenas [79] data as they also used the same form of characteristic length to calculate Kn. Since the formulation was chosen incorrectly for both sets of data, Kn was recalculated using Eq. 8.

To produce a blended model for particle C_D that can be implemented numerically, the experimental data given in Table 2 was compared to different empirical models, as given in Table 1, at the respective flow conditions. The best performing empirical model is identified by comparing model values with experimental data using the relative error

$$\epsilon_{\mathrm{r}} = \left| \frac{C_{D_{\mathrm{exp}}} - C_{D_{\mathrm{num}}}}{C_{D_{\mathrm{exp}}}} \right| \tag{25}$$

where $C_{D_{\mathrm{exp}}}$ and $C_{D_{\mathrm{num}}}$ are the experimental and numerical values of C_D, respectively. The values of ϵ_{r} were then examined for different Mach number regimes, allowing selection of the best performing empirical model along with the corresponding range of Re and Kn, where it produces the minimum value of ϵ_{r}. Note that some experimental data points produced values of $\epsilon_{\mathrm{r}} > 50\%$ and thus were not used for model selection. It should be noted that these excluded experimental data points constitute only about 3% of the total data.

To minimize discontinuities in the C_D predicted by the blended model, smoothing functions are applied at the interval values of Kn and Re between the empirical models used. For example, Model 1 and Model 2 are used for flows with Re or Kn less than and greater than N, respectively, where N is a numerical value. The smoothing function takes the form:

$$C_D = (1 - f)\, C_{D_1} + f C_{D_2} \tag{26}$$

where

$$f\left(N'\right) = \frac{\log(N') - \log(N - \Delta N)}{\log(N + \Delta N) - \log(N - \Delta N)} \tag{27}$$

Here, C_{D_1} and C_{D_2} represent the drag coefficients from Model 1 and Model 2, N' represents any value in the interval $[N - \Delta N, N + \Delta N]$. Based on the proximity of other interfaces, ΔN is chosen for each interface. The smoothing function, as shown in Eq. 26, converts the discontinuities to a smooth curve. In some instances, the discontinuities are still present. For example, there is a sudden discontinuous change in C_D when Kn crosses 1 for Eq. 16. In such cases, the C_D calculated using Eq. 26 is multiplied with a factor to bridge the discontinuity. The values used for factors are determined through numerical study and occur mostly for flows with M ranging between 1.7 and 5. The components of the blended C_D model are provided for the different Mach number ranges below. For most of the Mach number regimes, it was found that Eq. 18 works well for most of the cases. For the rest of the regions, Eq. 18 was replaced with other empirical models whose numerical values gave a better agreement with the experimental ones.

The flow conditions given in Table 2 and discussed in the following sections are those of the free-stream. These, however, are equivalent to relative flow conditions. The relative velocities in Aroesty's MM experiments [58] are equivalent to particle velocities, and the relative velocities in the rest of the experiments [80, 79, 58, 61, 77, 78], are equivalent to the free-stream velocity of the fluid.

3.0.1. Subsonic flow ($M \leq 0.8$)

Table 3 lists the blended model components used for subsonic flow ($\mathrm{M} \leq 0.8$). In this (still compressible) regime, Eq. 18 was found to best predict C_D over the widest Re range in the continuum regime, and at high Re in the slip regime. For Reynolds number below 2000, Eq. 16 was found to perform best for flows with $0.01 < \mathrm{Kn} < 0.04$, and Eq. 14 for flows with $0.04 < \mathrm{Kn} < 0.1$. No experimental data was found for the transition regime in subsonic flow. Because of its exclusive dependency on Kn, Eq. 16 was used in the transition regime.

Table 3: Drag coefficient model components for subsonic flow

Re	Kn	Eq. #
$\forall$Re	$\mathrm{Kn} < 0.01$	18
$\mathrm{Re} < 2000$	$0.01 < \mathrm{Kn} < 0.04$	16
$\mathrm{Re} < 2000$	$0.04 < \mathrm{Kn} < 0.1$	14
$\mathrm{Re} > 2000$	$0.01 < \mathrm{Kn} < 0.1$	18

The blended model prediction for C_D at $\mathrm{M} < 0.630$ are compared to the experimental data in Fig. 1. Figures 1(a) and 1(b) present the behavior of the model's C_D as a function of Re and Kn, respectively, for different Mach numbers. Figure 1(b) indicate continuum and slip regimes. As shown, the model matches well with the experimental data points for all Re and Kn available within the stated uncertainty. The most significant difference occurs at $\mathrm{Re} = 4000$ and $\mathrm{M} = 0.204$, where an error of 12% occurs.

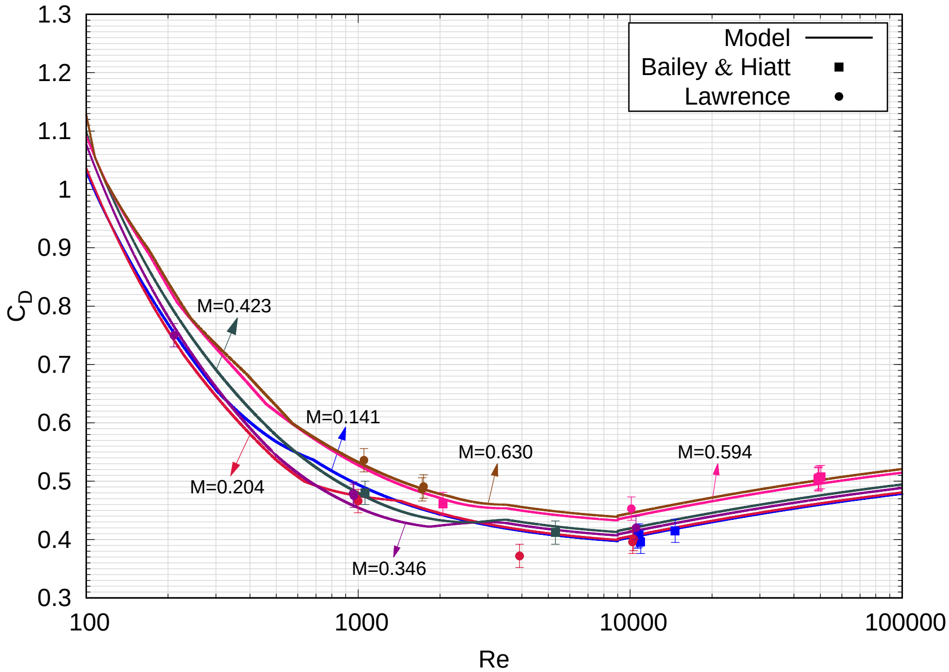

(a) C_D vs. Re

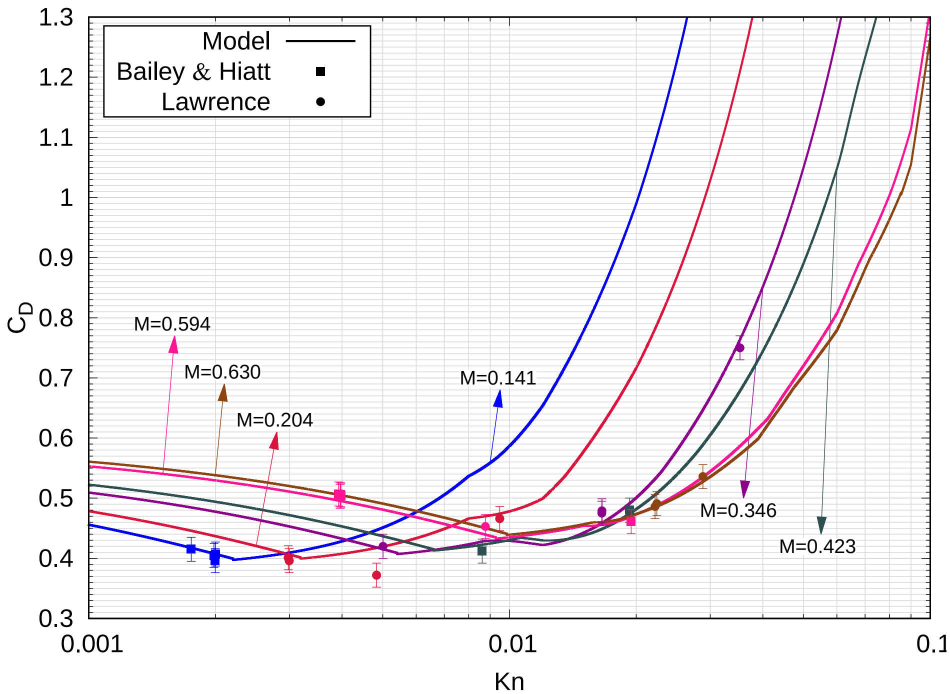

(b) C_D vs. Kn

Figure 1: Comparison between blended drag coefficient model and experimental data for subsonic flow (M $\leq$ 0.8). Different colors indicate different Mach numbers.

3.0.2. *Transonic flow* $(0.8 < M \leq 1.2)$

The transonic flow regime is divided into two parts: flow with Mach number below 1 and flow with Mach number above 1. The components of the blended C_D model for both regimes are presented in Table 4.

For transonic flow with M < 1, Eq. 18 was found to be a suitable model to predict the experimental results for both continuum and slip regimes, whereas Eq. 16 performed best for the transition regime. For transonic flow with M $\geq$ 1, Eq. 17 performed best for flows at higher Re values in slip regime (Kn > 0.03), whereas Eq. 16 performed best for flows in transition regime for Re < 200. Apart from that, C_D for the rest of the regions is predicted adequately with Eq. 16 and Eq. 18 for M < 1 and M > 1 flows, respectively.

Table 4: Drag coefficient model components for transonic flow

M	Re	Kn	Eq. #
0.8 < M < 1	∀ Re	Kn < 0.1	18
		Kn > 0.1	16
1 ≤ M < 1.2	∀ Re	Kn < 0.01	18
	Re < 1000	0.01 < Kn < 0.1	18
	Re > 1000	0.01 < Kn < 0.03	18
	Re > 1000	0.03 < Kn < 0.1	17
	Re < 200	Kn > 0.1	16
	Re > 200	Kn > 0.1	18

In Figs. 2 and 3, the blended model predictions for C_D are compared to the experimental data from Bailey and Hiatt [61] and Lawrence [77]. Figure 2 shows the results for Mach numbers spanning the range of $0.826 \leq$ M ≤ 0.973 and Fig. 3 shows the results for Mach numbers spanning the range of $1.013 \leq$ M ≤ 1.164. Figure 2(b) and 3(b) show slip and transition regimes. For transonic flow with M < 1 (Fig. 2), most of the experimental data points match well with the blended model, within the stated uncertainty of the experiment. The maximum error among the points in this range was 13%, which corresponds to the data from Lawrence [77] at M = 0.896. For transonic flow with M > 1, only the Bailey and Hiatt [61] data is available for comparison. As shown in Fig. 3, most of the data agree with the blended model, with the maximum error of 13% occurring for M = 1.164 and Re = 95.

3.0.3. *Supersonic flow* $(1.2 < M \leq 3.0)$

In order to increase the capability of the blended model for best prediction, the supersonic regime is divided, and M = 1.7 is arbitrarily selected for the division. The components of the blended model are provided in Table 5. For 1.2 < M $\leq$ 1.7, Eq. 18 was found to provide the best agreement with the experiments within the continuum, slip, and transition regimes when Kn < 0.08 and Eq. 17 for Kn > 0.08.

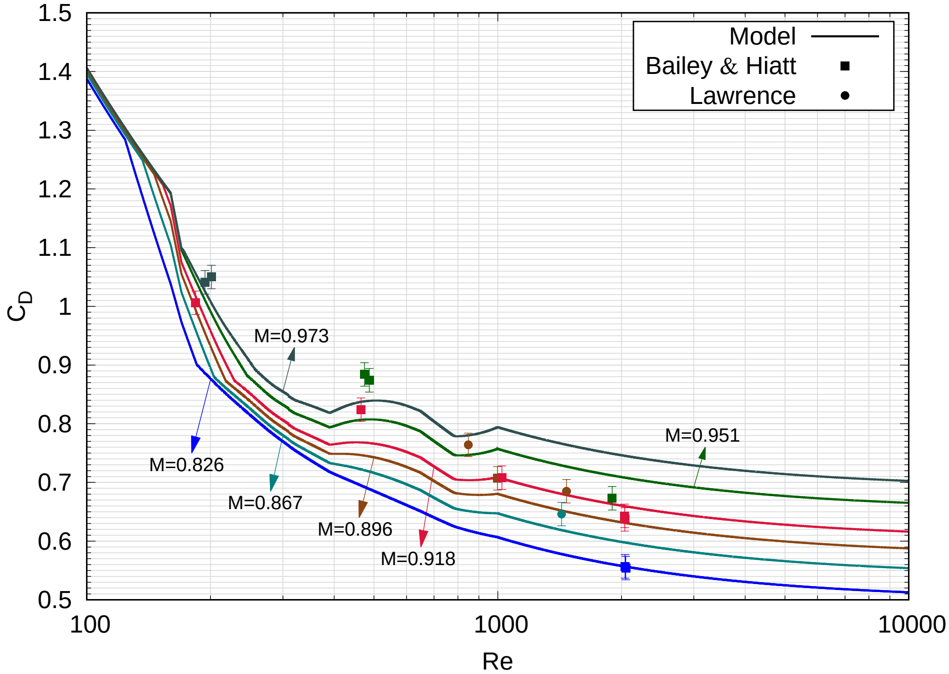

(a) C_D vs. Re

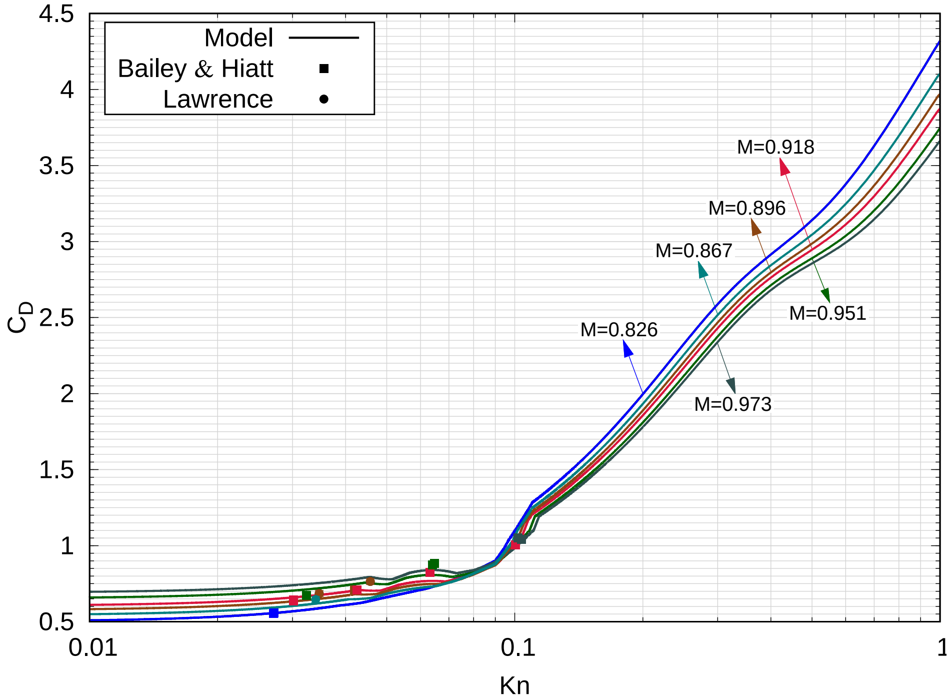

(b) C_D vs. Kn

Figure 2: Comparison between blended drag coefficient model and experimental data for transonic flow ($0.8 < \mathrm{M} \leq 1.0$). Different colors indicate the different values of Mach number.

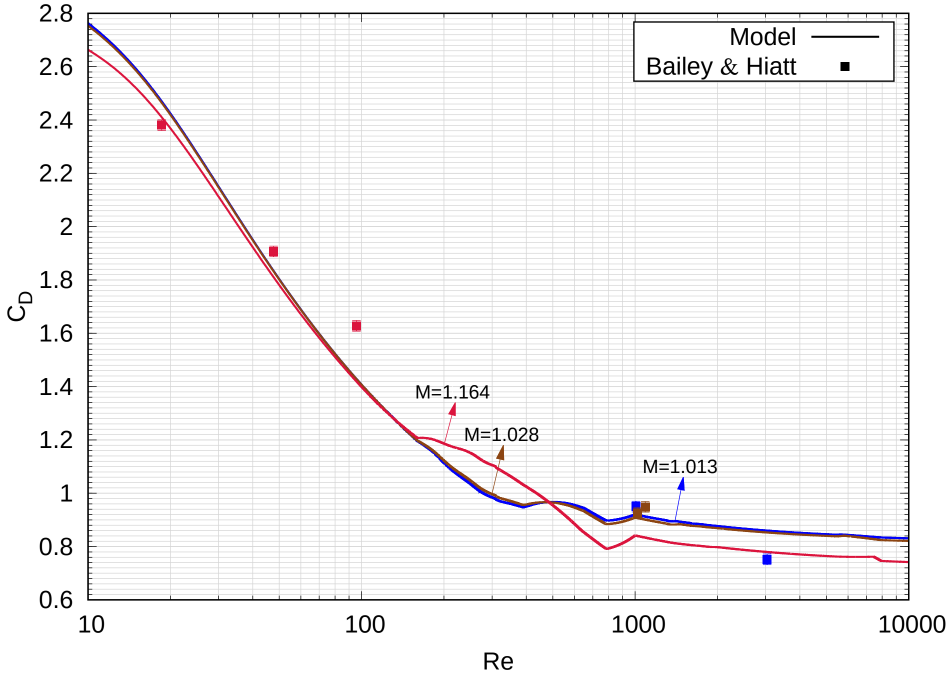

(a) C_D vs. Re

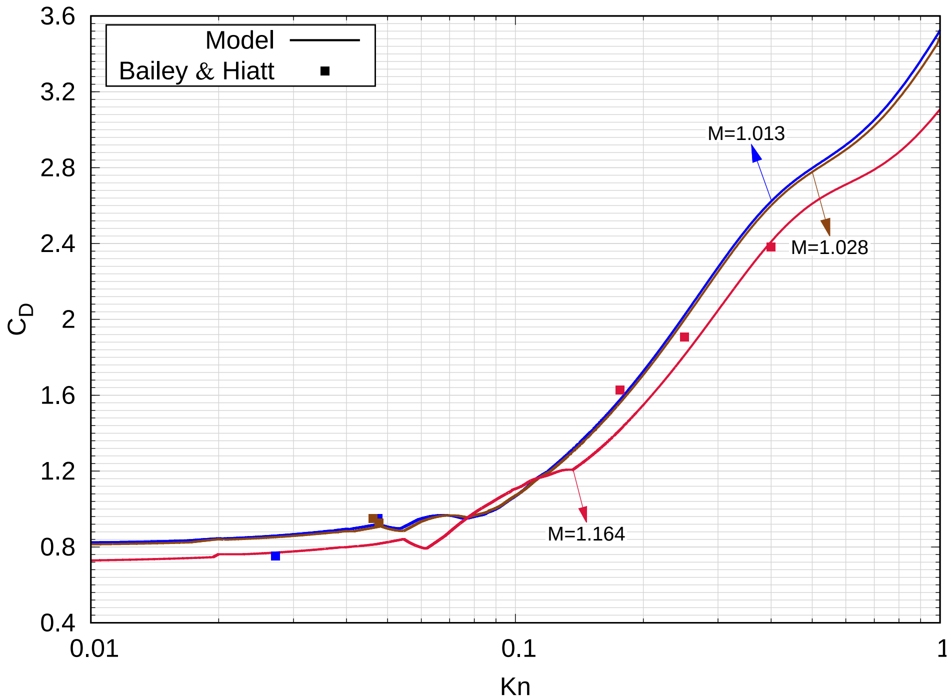

(b) C_D vs. Kn

Figure 3: Comparison between blended drag coefficient model and experimental data for transonic flow ($1.0 < \mathrm{M} \leq 1.2$). Different colors indicate the different values of Mach number.

For $1.7 < \mathrm{M} \leq 3.0$, Eq. 16 is used in transition regime for flows where $\mathrm{Re} < 20$ and $\mathrm{Kn} < 1$, and for flows where $20 < \mathrm{Re} < 100$ and $0.5 < \mathrm{Kn} < 0.6$. The other regions ranging from continuum to transition regimes perform well with Eq. 18.

Table 5: Drag coefficient model components for supersonic flow

M	Re	Kn	Eq. #
$1.2 < \mathrm{M} \leq 1.7$	$\forall$ Re	$\mathrm{Kn} < 0.08$	18
		$\mathrm{Kn} > 0.08$	17
	$\forall$ Re	$\mathrm{Kn} < 0.1$	18
	$\mathrm{Re} < 20$	$\mathrm{Kn} < 1$	16
	$\mathrm{Re} > 20$	$\mathrm{Kn} > 1$	18
$1.7 < \mathrm{M} \leq 3$	$20 < \mathrm{Re} < 100$	$0.1 < \mathrm{Kn} < 0.5$	18
	$20 < \mathrm{Re} < 100$	$0.5 < \mathrm{Kn} < 0.6$	16
	$\mathrm{Re} > 20$	$\mathrm{Kn} > 0.6$	18
	$\mathrm{Re} > 100$	$0.1 < \mathrm{Kn} < 0.6$	18

Figures 4 and 5 compare the blended model predictions for C_D within the supersonic regime to the experimental data from Bailey and Hiatt [61], Aroesty [58], Sreekanth [80], and Kane [78]. The model prediction for Mach numbers within the range $1.211 < \mathrm{M} < 1.698$ is shown in Fig. 4 and for $1.727 < \mathrm{M} < 2.991$ in Fig. 5. It should be noted that the Reynolds number dependence shows non-monotonic behavior within the range of $100 < \mathrm{Re} < 1000$. However, the model predicts the experimental data well, and the maximum error is 10% for a point from Bailey and Hiatt [61] data and for Mach number 1.474 at $\mathrm{Re} = 100$. At higher Mach numbers, as shown in Fig. 5, this non-monotonic behavior becomes less prevalent, and the maximum error is 10% corresponding to Aroesty [58] at $\mathrm{M} = 2.174$. Figure 4(b) and 5(b) indicate slip and transition regimes. The same non-monotonic behavior is also observed for Knudsen number dependence of C_D as shown in Fig. 4(b)

Two observations can made from Fig. 4. First, the C_D behavior is non-monotonic. Second, with an increase in M, C_D decreases at low Re and increases at higher Re. The drag from fore-body pressure, after-body pressure, and viscous components sum up to produce the total drag. The contribution of viscous drag decreases with an increase in Re and M and is minimal for flows above $\mathrm{Re} \approx 100$ [62, 81]. In the supersonic regime, the fore-body pressure drag decreases with an increase in Reynolds number until $\mathrm{Re} \approx 300$. After that, it remains relatively constant [81]. At high Reynolds number ($\mathrm{Re} > 10^4$), the fore-body pressure drag is a linear function of $1/\mathrm{M}^2$ and increases with an increase in M [82]. On the other hand, the after-body pressure drag increases with an increase in M until it reaches 1 [62]. After that, it shows a non-monotonic behavior at low Reynolds number and increases with Re and decreases with M [58, 83, 84]. The rise in after-body pressure drag is significantly smaller for flows above Re $= 2 \times 10^5$ [85]. The C_D reaches a maximum at a Mach number between 1.5 and 2, after which fore-body drag becomes the main contributor [50, 62]. Thus, at low Reynolds number, the viscous drag plays a significant role and decreases with M due to an increase in rarefaction effects [55]. On the other hand, at high Reynolds number, viscous drag is relatively small, and pressure drags play a significant role, which increases with an increase in M.

It should be noted that a point of intersection of all the C_D curves can be observed in Fig. 4. This behavior is due to Eq. 18, which has three sets of equations. For flows with $1 < \mathrm{M} < 1.75$, Eq. 18 linearly interpolates the values of C_D using the other two sets of equations. It is this interpolation equation that causes the intersection of the C_D curves. It is hypothesized that Henderson [72] introduced the interpolation equation to capture the transition of C_D variation with M from subsonic to supersonic flows.

3.0.4. *Hypersonic flow* ($M > 3.0$)

The hypersonic flow regime is divided into two parts: one where the Mach number is below 5 and another where the Mach number is above 5. For $3 < \mathrm{M} \leq 5$, Eq. 18 performs well for flows in regimes ranging from continuum to transition regimes, except for a region in transition regime for $\mathrm{Re} > 200$ and $0.33 < \mathrm{Kn} < 0.45$ where Eq. 17 performs well. On the other hand, for $\mathrm{M} > 5$ flows, Eq. 18 is used for continuum, slip, and transition regimes for $\mathrm{Kn} < 0.45$, and Eq. 17 is used for the flows with $\mathrm{Kn} > 0.45$.

Table 6: Drag coefficient model components for hypersonic flow

M	Re	Kn	Eq. #
	$\forall$ Re	$\mathrm{Kn} < 0.1$	18
	$\mathrm{Re} < 200$	$\mathrm{Kn} > 0.1$	18
$3 < \mathrm{M} < 5$	$\mathrm{Re} > 200$	$0.1 < \mathrm{Kn} > 0.33$	18
	$\mathrm{Re} > 200$	$0.33 < \mathrm{Kn} < 0.45$	17
	$\mathrm{Re} > 200$	$\mathrm{Kn} > 0.45$	18
$\mathrm{M} > 5$	$\forall$ Re	$\mathrm{Kn} < 0.45$	18
	$\forall$ Re	$\mathrm{Kn} > 0.45$	17

Figure 6 presents the model for Mach number below 5 and Fig. 7 presents the model for Mach number above 5 along with experimental data points from Bailey and Hiatt [61], Aroesty [58], and Wegener [79]. The Mach numbers considered for Fig. 6 are within the range of $3.083 \leq \mathrm{M} \leq 4.957$, and those for Fig. 7 are $5.193 \leq \mathrm{M} \leq 5.989$. Figure 6(b) and 7(b) both indicate transition regime.

Figure 6 shows that most of the points match well with the model, and the maximum error is 10%, for the points reported by Bailey [61], for a Mach number of 4.957. However, for the latter part of the hypersonic

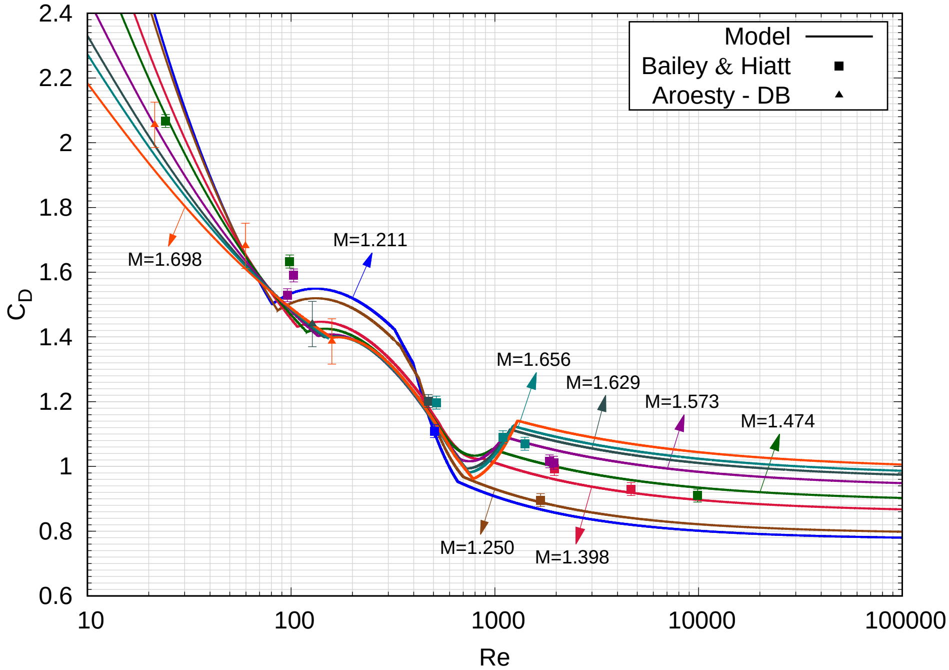

(a) C_D vs Re

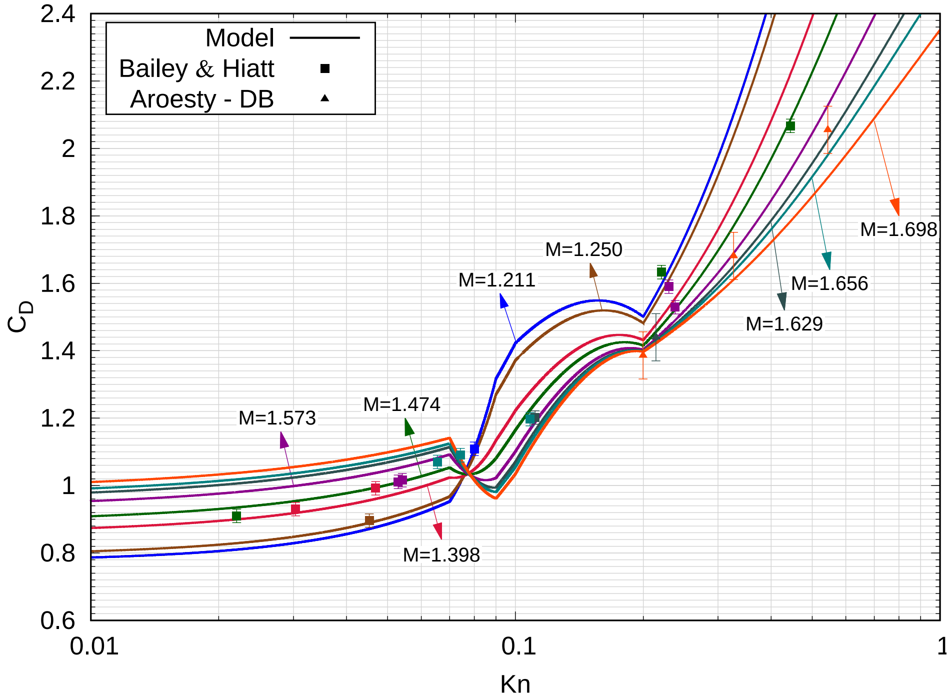

(b) C_D vs Kn

Figure 4: Comparison between blended drag coefficient model and experimental data for supersonic flow ($1.2 < \mathrm{M} \leq 1.7$). Different colors indicate different Mach numbers.

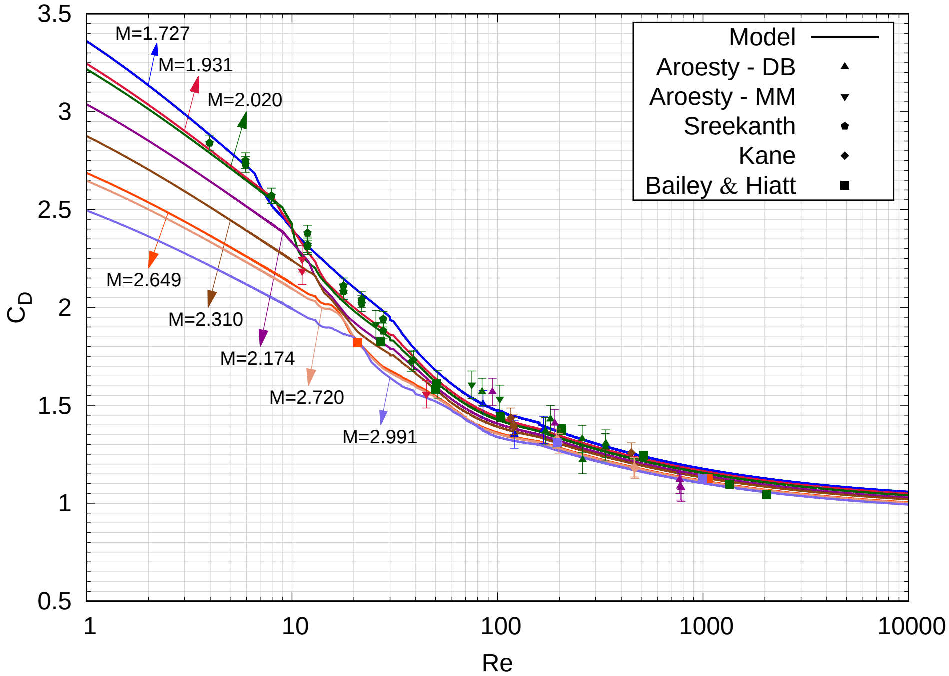

(a) C_D vs Re

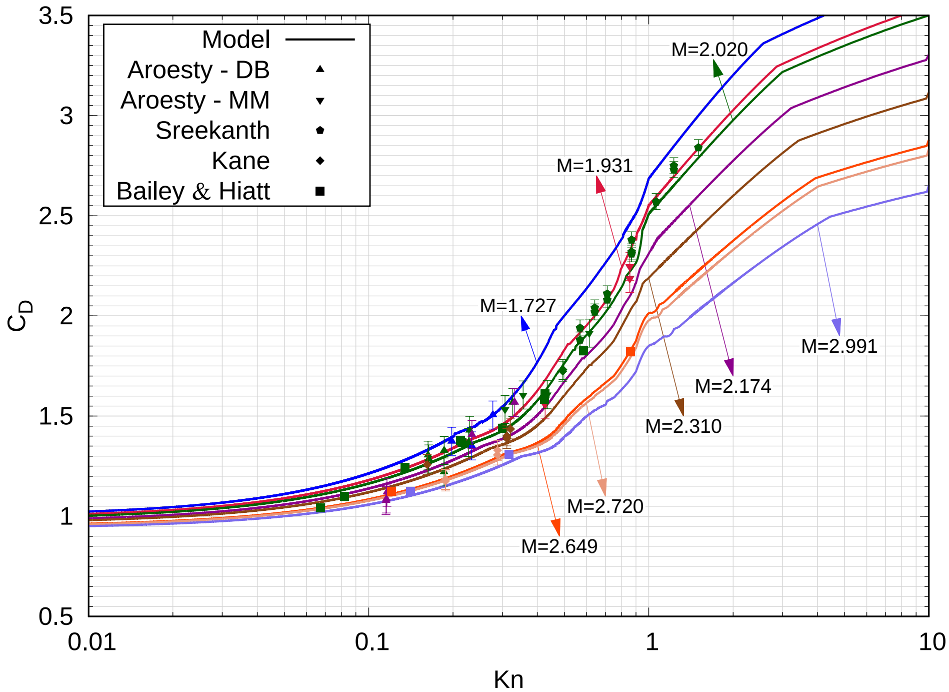

(b) C_D vs Kn

Figure 5: Comparison between blended drag coefficient model and experimental data for supersonic flow ($1.7 < \mathrm{M} \leq 3.0$). Different colors indicate different Mach numbers.

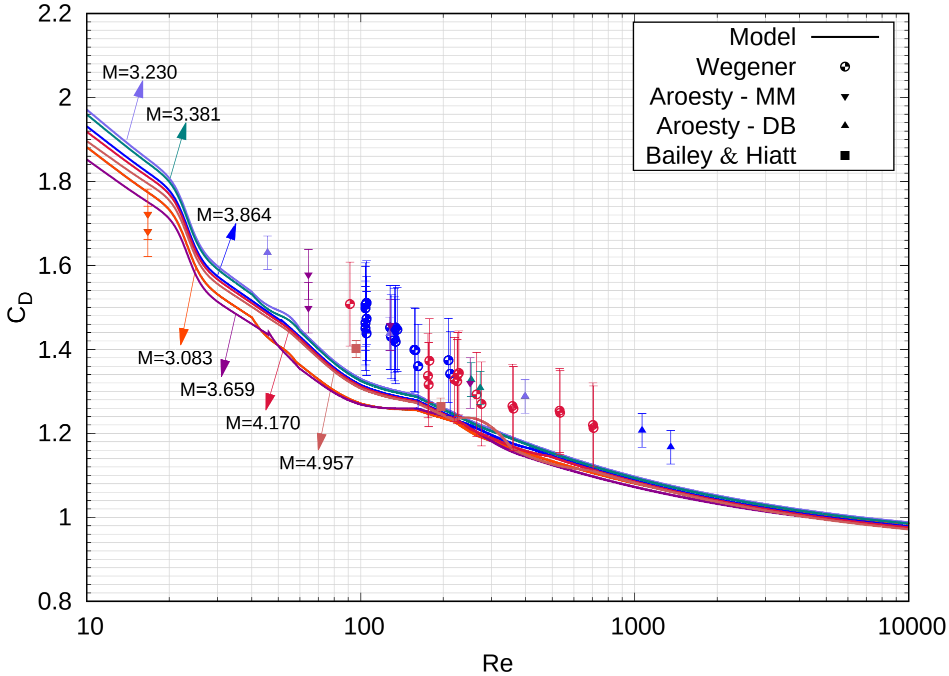

(a) C_D vs Re

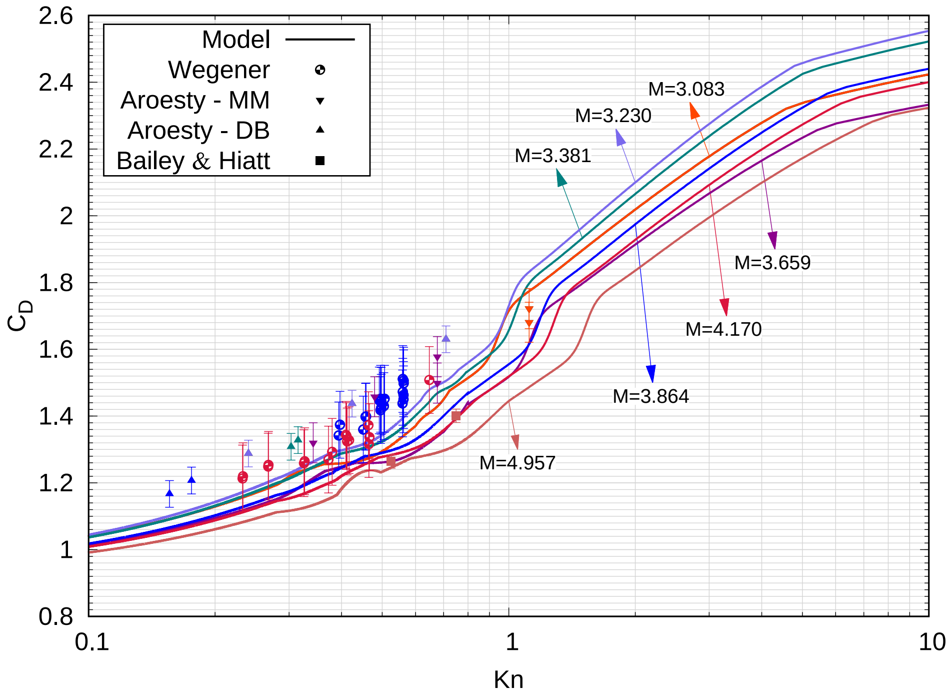

(b) C_D vs Kn

Figure 6: Comparison between blended drag coefficient model and experimental data for hypersonic flow ($3.0 < \mathrm{M} \leq 5.0$). Different colors indicate different Mach numbers.

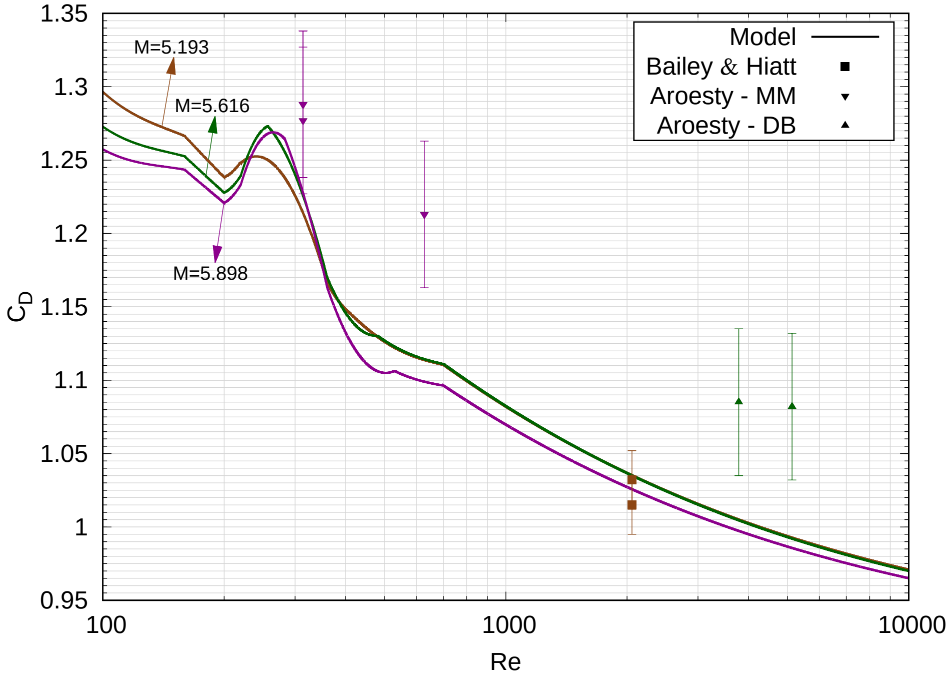

(a) C_D vs Re

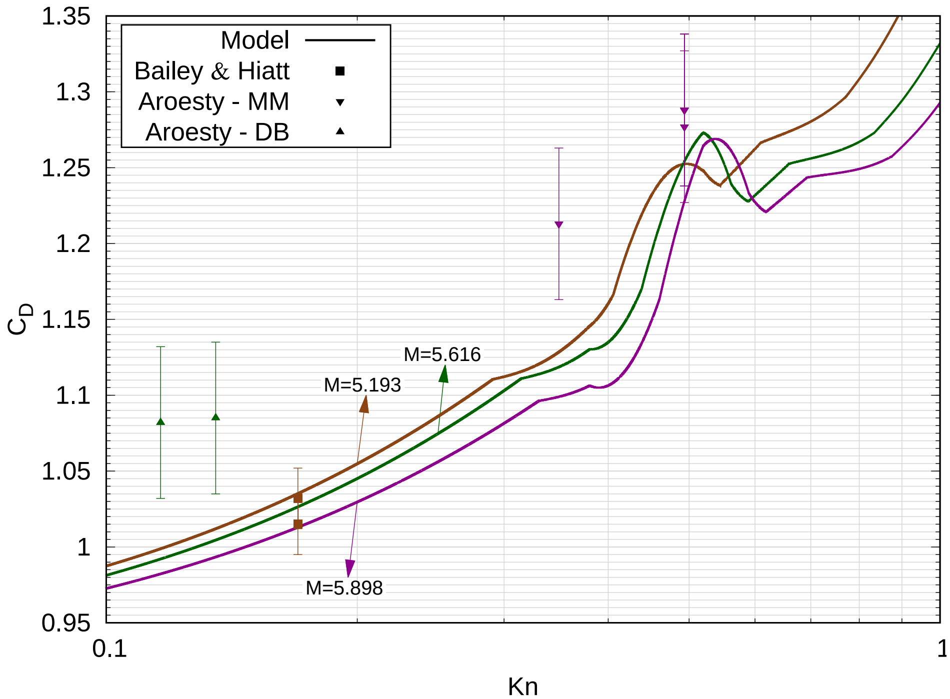

(b) C_D vs Kn

Figure 7: Comparison between blended drag coefficient model and experimental data for hypersonic flow (M > 5.0). Different colors indicate different Mach numbers.

regime, it was observed that the error was consistently higher for all the data points. The maximum error for this case is 9%, corresponding to Aroesty [58] MM data, for M = 5.898.

4. Blended model uncertainty

To quantify the uncertainty of the blended model, we use the relative errors between the model and each set of experimental data, including the uncertainty errors. The error is defined as

$$\epsilon = \begin{cases} 0, & \text{if } \epsilon_{\mathrm{r}} < \epsilon_{\mathrm{u}} \\ \epsilon_{\mathrm{r}} - \epsilon_{\mathrm{u}}, & \text{if } \epsilon_{\mathrm{r}} \geq \epsilon_{\mathrm{u}}. \end{cases} \tag{28}$$

The error ϵ represents the deviation in the percentage of the model for every set of experimental data. Both a standard percentage deviation (SD) and maximum percentage deviation in errors are calculated. A mean value for all the ϵ values, from every set of experimental data, is calculated. Then, an average of squared differences of all ϵ from the calculated mean is calculated for each set. The square root of this new average is then used as the SD of the respective data set. The maximum of all the ϵ's yields the maximum percentage deviation.

The maximum error and SD for each set of experimental data calculated using Eq. 28 is given in Table 7. Moreover, all the data from each set of experiments are merged into one final set, and the maximum error and SD were calculated for it. It is inferred from the calculations that the SD of the model is 2.84%. The calculated SD value indicates that the ϵ of all the experimental data is distributed close to the mean (=2.48%). A low SD value demonstrates the reliability of the model when predicting the value of the drag coefficient. It is also noted that the maximum percentage deviation is 11.87%. Henderson [72] did a similar study by comparing his and Carlson & Hoglund's model [71] to several experiments [61, 73, 86]. Henderson concluded that the maximum percentage deviation for Carlson & Hoglund model is 117% and for Henderson model 16%. On the other hand, the blended drag model presented here has a lower maximum percentage deviation of 11.87% and is validated by comparing with a greater number of experiments that covers a wider range of M, Re, and Kn numbers.

The best way to quantify the error in the drag coefficient model is to compare the computed particle motion with the experimental data. The following sections assess the validity of the model by comparing the velocity and trajectories of particles to experimental data [87, 70, 88].

5. Validation of Particle Trajectory Model

To predict the trajectory of the particle, Re, Kn, and M are used to find C_D at that instant in time using the blended model described in Section 3. The net resulting force on the particle can then be found through

Table 7: Statistics of errors between the model and experiment

Experiment	SD	Maximum error
Kane [78]	2.70%	9.10%
Wegener and Ashkenas [79]	0.72%	4.79%
Sreekanth [80]	2.50%	8.83%
Aroesty-DB [58]	2.56%	10.38%
Aroesty-MM [58]	3.37%	11.10%
Lawrence [77]	3.12%	10.72%
Bailey and Hiatt [61, 51]	2.56%	11.87%
All	2.84%	11.87%

Eq. 5 and Eq. 4, which is then inserted into $\mathbf{W}$ of Eq. 1 to determine the momentum change of the particle. The system of equations represented by Eq. 1 is solved that calculates mass, velocity, and temperature of the particle for each time step. The velocity of the particle is equal to the rate of change of position. The discretized version is inserted in Eq. 1 and also solved to obtain the position of the particle.

To validate the particle trajectory model, we compare the predicted velocity (Section 5.1) and the trajectory (Section 5.2). The experiments chosen use supersonic flows over wedge samples.

Flows that have large velocity gradients provide an opportunity to measure the dynamics of the particle. It is particularly true for flows containing an aerodynamic shock. Upstream of the shock, one can assume the particle velocity matches that of the fluid and $\mathbf{V_r} = 0$. However, when crossing the shock, there is an abrupt change in flow velocity. However, the inertia of the particle prevents it from responding instantly. In the downstream region, the velocity of the particle is initially the same as the upstream velocity. At this point, $\mathbf{V_r} \neq 0$ and is referred to as the particle slip error, and the distance the particle travels before $|\mathbf{V_r}|$ is less than 1% of the surrounding fluid velocity ($|\mathbf{V_f}|$) is defined as the relaxation distance.

A compressible flow, with a Mach number greater than 1, over an inclined surface such as a wedge, produces an oblique shock and an expansion fan. When a particle passes through this region, it encounters a range of velocity gradients, which is a suitable domain not only for measuring the dynamics but also to test a particle trajectory model. As the particle travels through the relaxation distance, it experiences significant changes in its dynamics, and it is seen that these changes magnify the errors of the model.

The tracer particles employed in the experiments used for validation were non-reactive. Therefore, the chemical interactions of the particles are not taken into consideration.

5.1. Velocity

The experiments performed by Thomas et al. [87, 45] and Tedeschi et al. [70, 47, 46] were used to validate the model velocity prediction.

Thomas et al. [87] used seeding particles of a known diameter in a supersonic flow over a wedge sample and measured their average velocity using laser doppler anemometry (LDA). The experiments were conducted for three different wedge samples with half-angles of 6.3°, 12°, and 14°. Different types of seeding particles were also used: atomized olive oil, incense smoke, Titanium oxide (TiO_2), and "Blanc Fixe, Micro" (refined $BaSO_4$). The experiment using "Blanc Fixe, Micro" as seeding particles was only performed for M = 1.95 in air, over a wedge with a half-angle of 14°, and is considered here for validation. The test conditions for the experiment are given in Table 8, and the test geometry is shown in Fig. 8(a). Table 8 lists the values of temperature (T_∞), density (ρ_∞), mass fractions (Y), velocity (V_∞), and Mach number (M_∞) of air in the free-stream (or upstream) and the wall (or surface) temperature (T_w) of the wedge.

Tedeschi et al. [70] used LDA to measure seeding particle velocities in a supersonic flow. However, in this case, the flow was over the shock generator. The shock generator consisted of a plate that is inclined at an angle of 8° in the free stream direction, as illustrated in Fig. 8(b). The seeding particles used for the experiments were incense smoke and latex spheres. The uncertainty for experiments was given as 0.1% in the x-direction and 4% in the y-direction. For the validation, the experimental results obtained using latex spheres as seeding particles for a flow of M = 2.3 and total pressure of 0.5×10^5 in the air were considered. The test conditions for the experiment are given in Table 8.

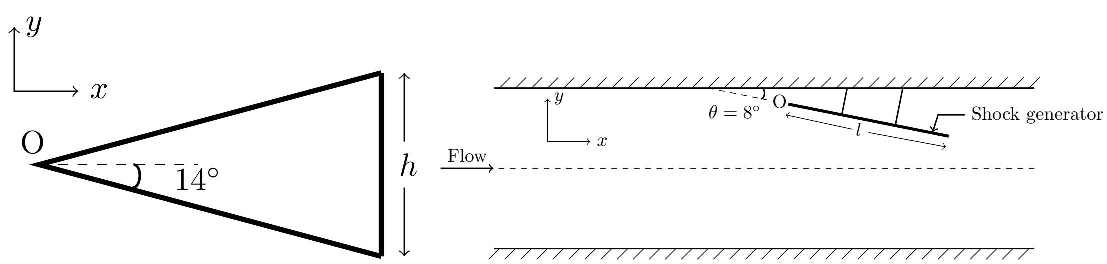

(a) Thomas et al.

(b) Tedeschi et al.

Figure 8: Wedge sample used by Thomas et al. [87] (where h = 0.07 m) and wind-tunnel setup for experiment used by Tedeschi et al. [70] (where $l = 0.167$ m) where "O" is the origin.

To validate the particle trajectory model, the converged steady-state CFD solutions were computed using KATS for test conditions of both the experiments, as given in Table 8. The flow field data was extracted and used in the particle trajectory code to determine V_p velocity profiles. For the simulation, the average size of the seeding particles in the respective experiments and the free-stream conditions of the flow were taken as initial values. Single-particle simulation is performed, and the particle's velocity variation with respect to

Table 8: Test conditions of LDA experiments

Experiment	T_∞, K	ρ_∞, kg/m^3	Y_{N_2}	Y_{O_2}	V_∞, m/s	M$_\infty$	T_w, K
Thomas et al. [87]	167.0	0.2804	0.7671	0.2329	505.92	1.95	295.2
Tedeschi et al. [70]	147.0	0.0956	0.7671	0.2329	559.20	2.30	303.0

its position in the x-direction is compared with the experimental data.

The solution of the flow field for the experiments of Thomas et al. [87], obtained using KATS, is presented in Fig. 9(a). The solution of the flow field for the shock generator experiment of Tedeschi et al. [70] is shown in Fig. 9(b). It is to be noted that both flow field solutions presented in Fig. 9 are grid-independent. The velocity measurements for the Tedeschi et al. [70] experiment were performed across the region of oblique shock wave induced by the inclined shock generator. Since the flow over the inclined surface is equivalent to the flow over a wedge with 8° half-angle, the latter was used to simulate the flow field. Fig. 9(a) shows the flow velocity across the wedge where the velocity decreases from free-stream after the oblique shock and increases to free-stream (and more) as it goes through the expansion fan. Although the same general behavior is observed in Fig. 9(b), the flow velocity does not decrease as much in the region between oblique shock and expansion fan due to the large size of the wedge.

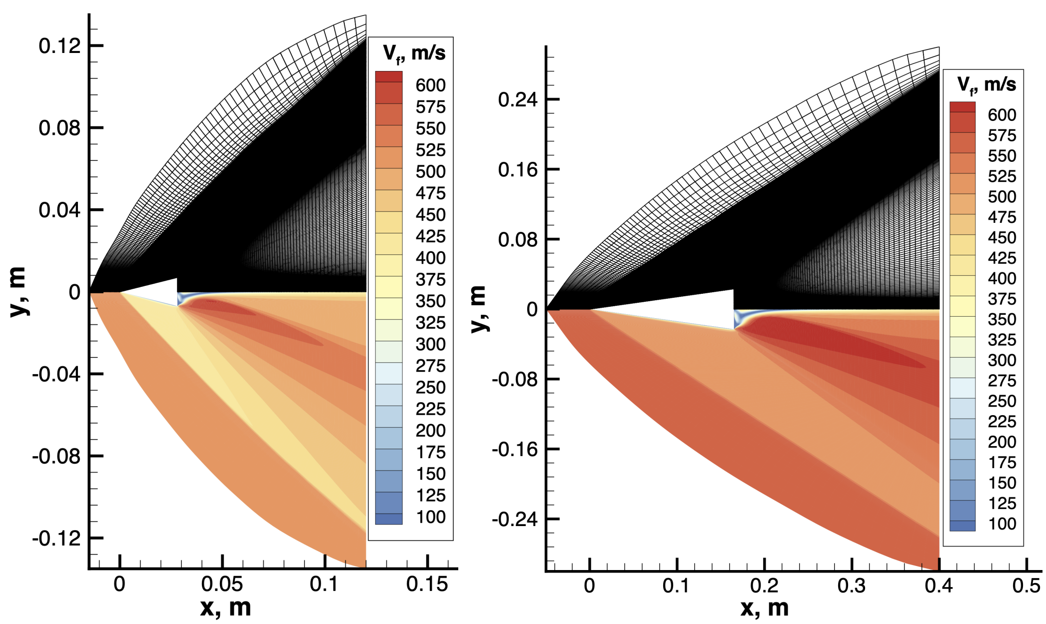

(a) Thomas et al. [87]

(b) Tedeschi et al. [70]

Figure 9: Velocity contours of the simulated flow field solution corresponding to test conditions of the experiments.

Thomas et al. [87] used "Blanc Fixe, Micro" particles with an average size of 0.7 μm and a density of 4400 kg/m^3, and the same values were used for simulation. These particles are of the same magnitude when compared to those present in rocket nozzle flows ($0.1 - 10$ μm) [89, 90] as well as those in Martian dust ($0.1 - 1$ μm) [4, 5] . Figure 10 compares the results of the simulation to the experiment for the velocity of the particle.

In Fig. 10(a), the experimental results indicate that the velocity of the particle decreases and increases near the shock location. However, it should be noted that this fluctuation is not physical, and was attributed to the optical distortion of the LDA beams caused by the shock [87]. Since the vertical velocity at this location is low, the measurements do not see any such fluctuations in the vertical direction, as shown in Fig. 10(b). For both vertical and horizontal velocity components, the numerical model produces excellent agreement with the experimental results.

Tedeschi et al. [70] used latex particles with an average size of 0.523 μm and a density of 1050 kg/m^3, and the simulation uses the same values. The results for the longitudinal velocity and transversal velocity are presented in Fig. 11. It is observed that simulated results show good agreement in predicting the Tedeschi et al. [70] results. Figure 11(a) shows that for the longitudinal velocity, the simulated trajectory agrees well with the experimental data. Similarly, the transversal velocity of both simulation and experiment match each other well, as seen in Fig. 11(b).

The location of velocity measurements for each experiment was at a transversal distance from the center axis of the wind tunnel ranging from upstream to downstream (after the expansion fan) of the shock. Therefore, these experimentally measured velocities are a function of specific locations in space. On the other hand, the particle model follows a Lagrangian frame reference, and the simulated trajectory does not necessarily pass through all the measurement locations. However, it was observed that the maximum difference between the trajectory and measurement points was of the order of magnitude 10^{-3} m for both Thomas et al. [87] and Tedeschi et al. [70] experiments. Figure 12 shows the location of measurement points and simulated trajectories based on Thomas et al. [87] and Tedeschi et al. [70] experimental conditions. The variation of simulated flow field velocity ($\mathbf{V_f} - \mathbf{V_\infty}$), for both Thomas et al. [87] and Tedeschi et al. [70], are also provided in Fig. 12, and illustrates the abrupt change in the value after the shock. Since the simulated points were very close to the measurement points, it can be inferred that the velocities predicted by the model closely resemble the experimental ones.

It should be noted that, irrespective of the free-stream flow regime, the particle's Mach number $\mathrm{M_p}$ ($= \mathrm{M_r}$) starts from 0 and increases to subsonic, then to transonic, and so on when it crosses the shock or ejects from a surface. Figure 13 illustrates the simulated $\mathrm{Re_p}$, $\mathrm{M_p}$, and $\mathrm{Kn_p}$ based on Thomas et al. [87] and Tedeschi et al. [70] experimental conditions. It can be seen that as the particle travels and crosses the shock, $\mathrm{M_p}$ increases to 0.45 and 0.2 for Thomas et al. [87] and Tedeschi et al. [70], respectively. These points

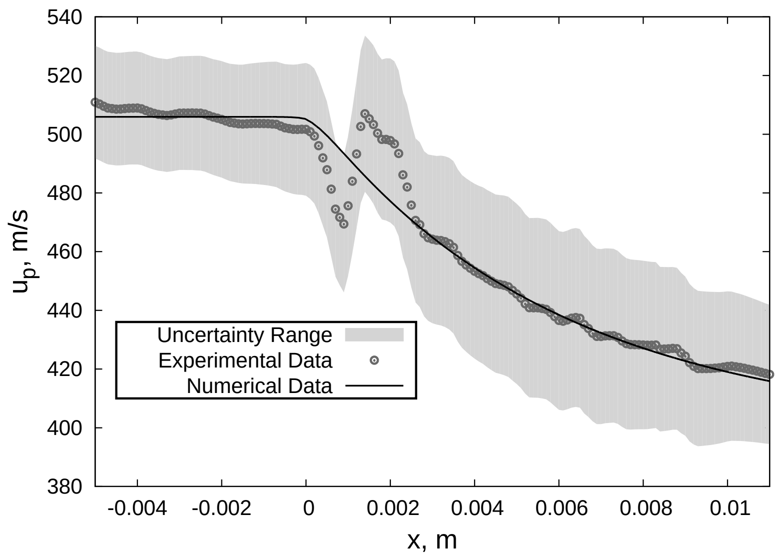

(a) Longitudinal velocity

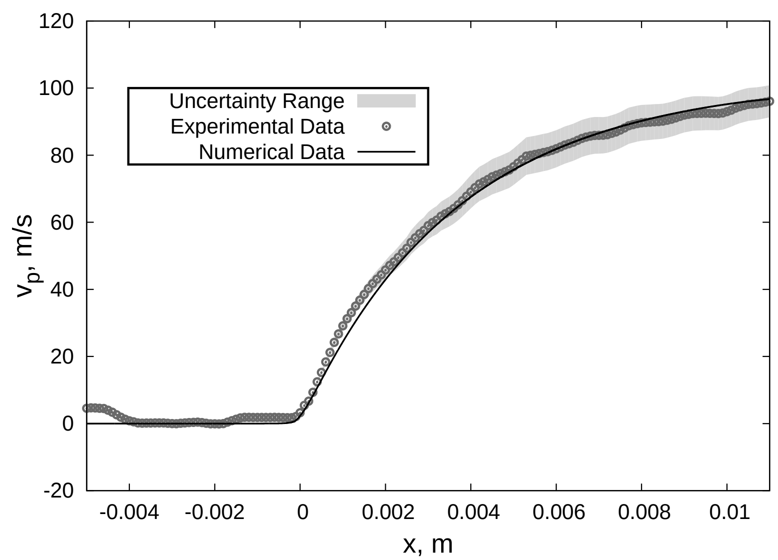

(b) Transversal velocity

Figure 10: Comparison of longitudinal and transversal components of particle's velocity between simulated and the experiments of Thomas et al. [87]. The uncertainty range was calculated by adding the stated experimental uncertainty to the average value of the velocity at every given location.

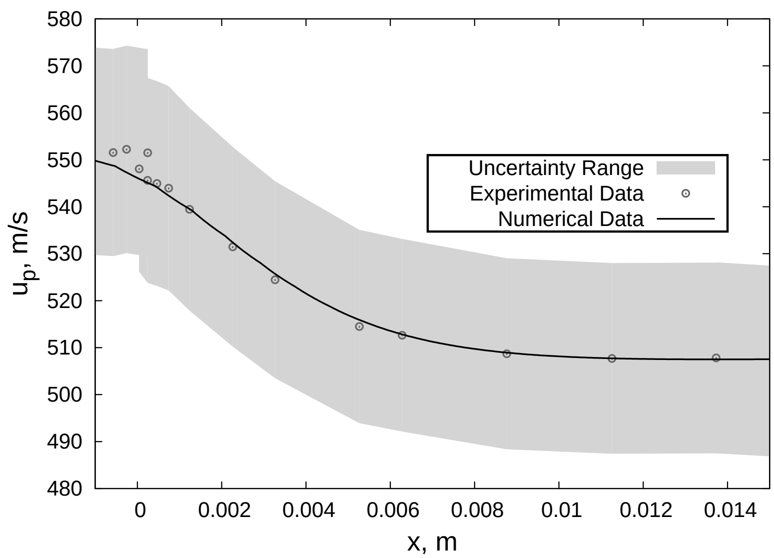

(a) Longitudinal velocity

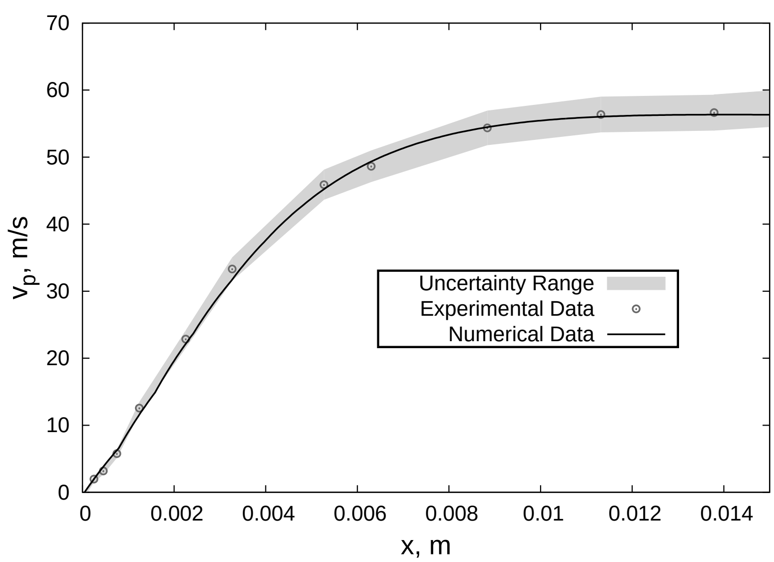

(b) Transversal velocity

Figure 11: Comparison of longitudinal and transversal velocity components of particle's velocity between simulated and experiments of Tedeschi et al. [70]. The uncertainty range is calculated by adding the error of 4% to the measured mean velocity values.

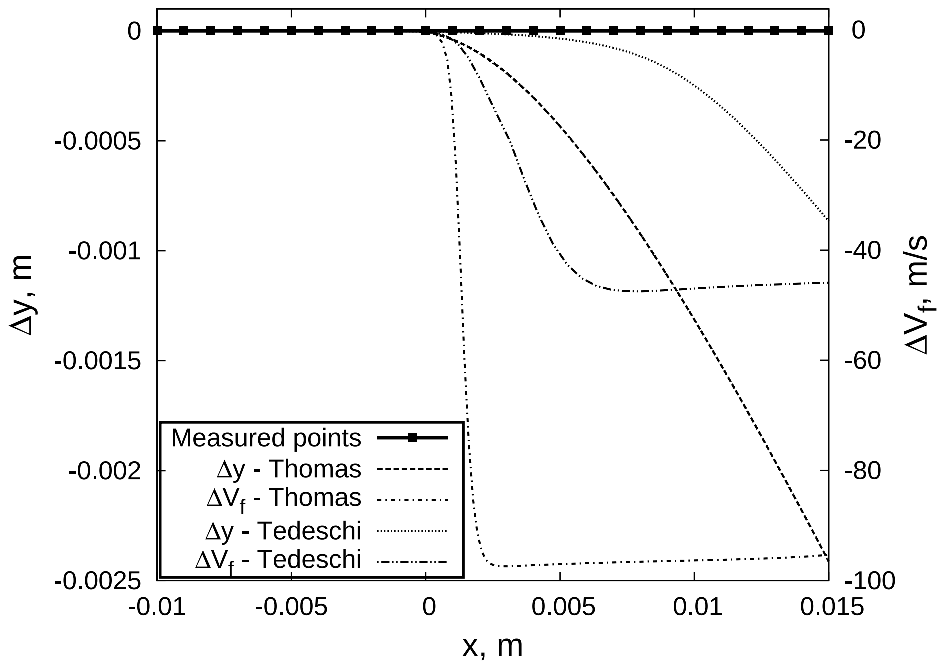

Figure 12: Comparison of simulated trajectories based on Thomas [87] and Tedeschi [70] experiments with respect to location of measurement points.

of maximum $\mathrm{M_p}$ denote the downstream regions after the shock, as can be seen by $\mathbf{V_f}$ profiles in Fig. 12. The $\mathrm{M_p}$ profiles then decrease before the particle adapts to the flow field velocity. Similarly, $\mathrm{Kn_p}$ changes from a free-stream value and decreases while the particle crosses the shock. As the particle travels through an expansion fan, $\mathrm{M_p}$ and $\mathrm{Kn_p}$ again increase to different values and follow the same behavior after that. It is interesting to note that even though $\mathrm{M_p}$ and $\mathrm{Re_p}$ are zero in the free-stream region, $\mathrm{Kn_p}$ has a constant value which can be calculated by inserting Eq. 6 and 7 into Eq. 8 to obtain

$$\mathrm{Kn_p} = \lim_{|\mathbf{V_r}| \to 0} \frac{\mathrm{M_p}}{\mathrm{Re_p}} \sqrt{\frac{\pi\gamma}{2}} = \frac{\mu_\infty}{\rho_\infty d_p a_\infty} \sqrt{\frac{\pi\gamma}{2}} \tag{29}$$

where ρ_∞, a_∞, μ_∞ represent free-stream density, speed of sound, and dynamic viscosity of the fluid, whereas d_p is the particle size. As the particle travels through the computational domain of the flow field as shown in Fig. 9, for both the experiments, the simulation shows that the particle is in transition regime, and $\mathrm{Kn_p}$ ranges between 0.2 and 0.8 for Thomas et al. [87] and between 1 and 4.5 for Tedeschi et al. [70].

The results, as shown in Fig. 10 and 11, suggest that the trajectory model captures the velocity changes accurately – despite the particle being in non-continuum regime – and successfully reproduces the particle velocities with $\mathrm{M_p}$ in the subsonic regime.

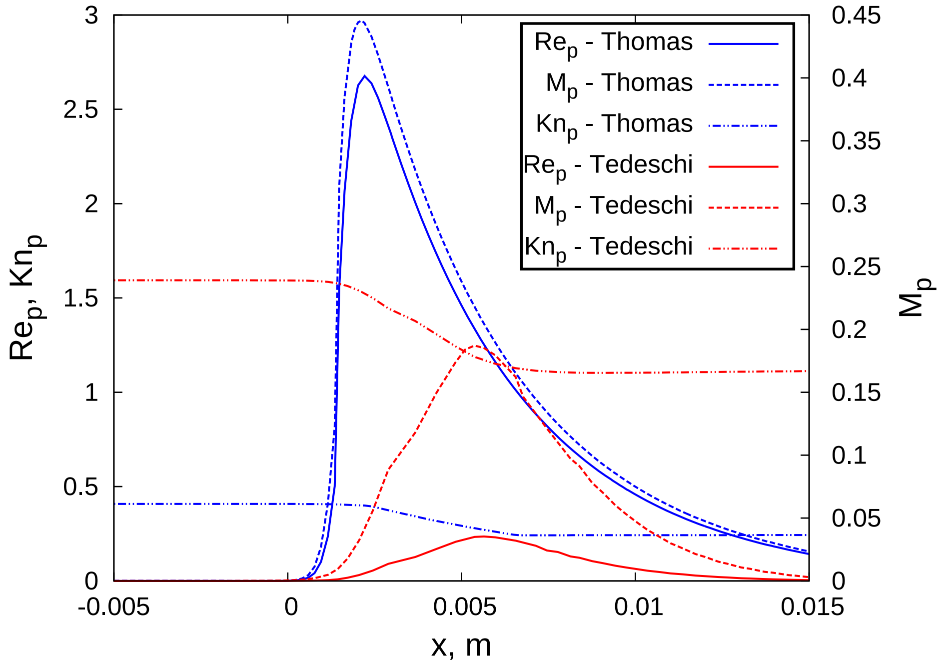

Figure 13: Variation of Reynolds number, Mach number, and Knudsen number of particles travelling through flow fields based on Thomas [87] and Tedeschi [70].

5.2. Trajectories

The comparison of the measured particle velocity with simulated results is not sufficient to evaluate the accuracy of the trajectory model. It is also necessary to extend the validation to particle trajectories. The experimentally determined particle trajectories can show an accumulation of error due to uncertainty in velocity measurements. The comparison with the simulated trajectory and its closeness to the experimental one determines the capability of the trajectory model in predicting the particle path and its properties.

In order to validate the particle trajectories, the velocity measurements conducted by Ross et al. [88, 91] were used. The measurements were obtained using Particle Image Velocimetry (PIV) and examined the slip velocity of flow around a wedge. The experiments were performed in a high-speed blowdown wind tunnel, and a converging-diverging axisymmetric nozzle was used to produce uniform free-stream of velocity $\mathrm{M} = 2$. Four different wedge samples were used in the experiment, shown in Fig. 14. They had the same base thickness (h), but with different half-angles ($5°$, $10°$, $15°$, and $22.5°$). It can be seen that the size of the wedge samples decreases with the increase in the half-angle of the wedge. For these experiments, aluminum oxide (Al_2O_3) powder was used as the seeding material.

Ross et al. [88] calculated the flow pathlines by integrating the velocity data from the experiments. An imaginary particle position in the upstream region was initially considered, with the velocity interpolated

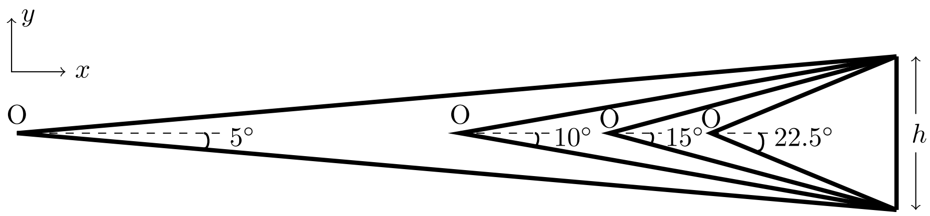

Figure 14: Configuration of 5°, 10°, 15°, and 22.5° half angle wedge airfoils with a constant base thickness h (= 0.25 in) where "O" is the origin.

Table 9: Test conditions of PIV experiments

Case	T_∞, K	ρ_∞, kg/m^3	$Y_{\mathrm{N_2}}$	$Y_{\mathrm{O_2}}$	V_∞, m/s	M_∞	T_w, K
1	160.0	2.197	0.7671	0.2329	508.076	2.0	288.71
2	295.5	1.210	0.7671	0.2329	690.338	2.0	533.15

from the data. At a Δt later, the velocity and position were calculated from the initial position, and the calculation procedure repeated until the particle crossed the data region. The experiments were conducted for the test conditions given in Table 9. While keeping the free-stream Mach number as 2, the two tests were conducted by changing the total temperatures (T_w), which in turn changed the free-stream temperatures (T_∞) and velocities (V_∞). It can be noticed from Table 9 that Case-1 represents a low-temperature flow, whereas Case-2 corresponds to a heated flow. Though the free-stream Mach number is the same, the shock strength is different. The velocity and temperature gradients are high for Case-2 when compared to Case-1. Thus, the particles traveling in Case-1 have a higher Re and lower Kn and, therefore, a different C_D.

The errors in the experiments, as given by Ross et al. [88], were typically 3%. Therefore, the uncertainty range along the particle trajectory is calculated as

$$\epsilon_x = \sqrt{\left(\frac{x}{0.5}\right)(0.03)^2} \quad \text{and} \quad \epsilon_y = \sqrt{\left(\frac{y}{0.5}\right)(0.03)^2} \tag{30}$$

where (x, y) is the position of the experimental points, and 0.5 is the magnification factor used on the images to reduce the signal-to-noise ratio.

The steady-state solutions of the flow field over different wedge samples were simulated using KATS-CFD based on the test conditions in Table 9. The results of the grid-independent solutions are shown in Fig. 15. It can be seen in Fig. 15 that as the half-angle of the wedge increases from 5° to 22.5°, there is an increase in the velocity intervals across the sample. The maximum deflection angle for a Mach 2 flow is 22.9°, and therefore, the shock appears to be almost detached for the 22.5° half-angle wedge sample.

Both the simulation and the PIV experiments were conducted using an average particle size of 0.8 μm, and a density of 4000 kg/m^3. Figure 16 presents the simulated and experimental trajectories for different

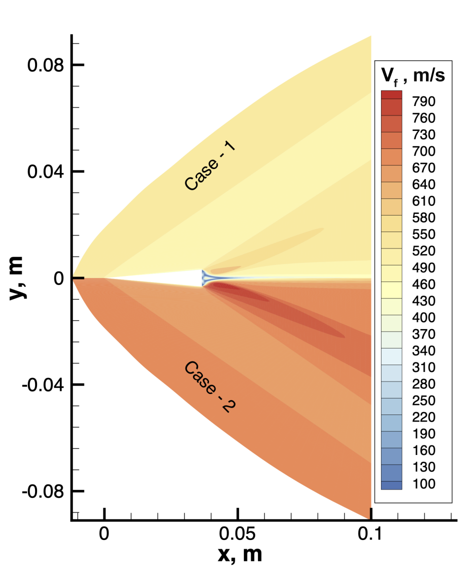

(a) 5° half angle wedge

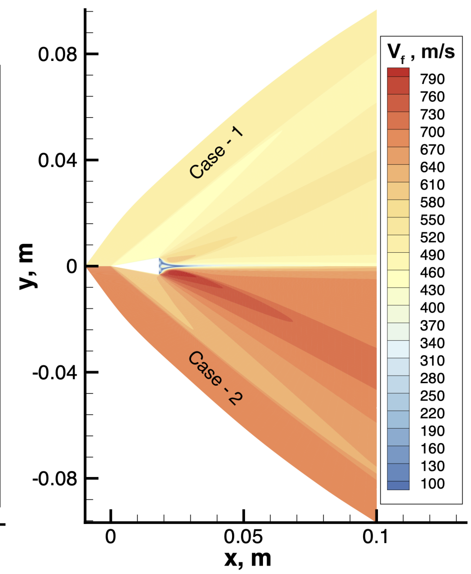

(b) 10° half angle wedge

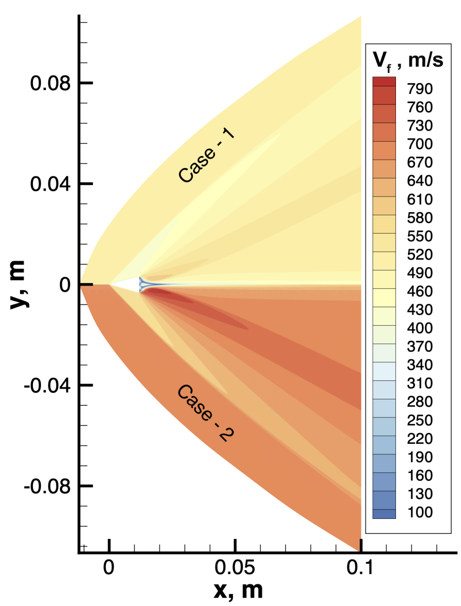

(c) 15° half angle wedge

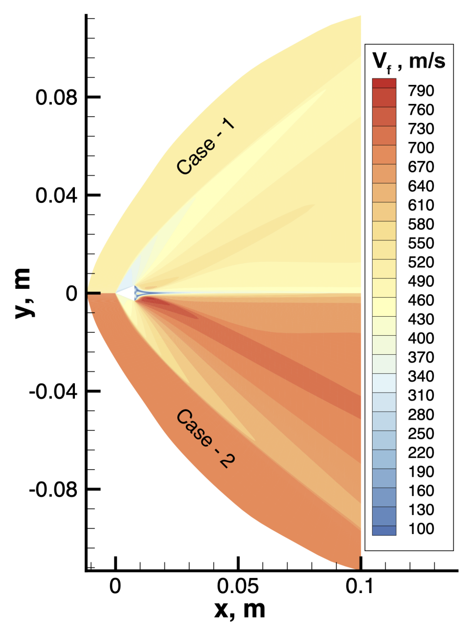

(d) 22.5° half angle wedge

Figure 15: Velocity contours of Mach 2 flow, for two test conditions, over 5°, 10°, 15°, and 22.5° half angle wedges

wedge samples. Figure 16(a) shows the trajectories for test conditions corresponding to Case-1, whereas Fig. 16(b) corresponds to Case-2.

It can be observed that the simulated trajectories pass through most of the PIV data points and are inside the uncertainty range for 5°, 10°, and 15° half-angle wedge samples. However, there seems to be a disagreement for the 22.5° half-angle wedge sample in both cases. Maxwell and Seasholtz [92] conducted studies that claimed that the relaxation distance for flows with normal Mach numbers, ahead of the shock, ranging from 1.15 to 1.43, was relatively constant. Based on the measured data of other samples, it was noted that the size of the 22.5° half-angle wedge sample is of the same order as the relaxation length of the particles. This resulted in particles reaching the re-accelerating region of the expansion fan before they could adapt to the velocity change in the fluid, thus producing a relaxation error. These particle relaxation errors caused the overlapping of velocity vectors, giving inconsistent measurements for velocity after the shock. Due to skewed velocity measurements for the 22.5° wedge sample, the pathline calculated did not accurately depict the path traversed by the tracer particle.

Other than the skewed data for the 22.5° wedge sample, the particle-tracking code was able to match the trajectories for other samples accurately, for both cases. Therefore, it can be implied that the simulated trajectory for a 22.5° wedge sample resembles the one followed by the tracer particle.

Similar to Fig. 13, Fig. 17 show the range of $\mathrm{Re_p}$, $\mathrm{M_p}$, and $\mathrm{Kn_p}$ for the test-cases used to validate the particle trajectories. These plots show that the particles travel from slip regime to transition regime with Kn ranging from 0.02 to 0.14 for Case-1 and from 0.06 to 0.22 for Case-2, respectively. The behaviors of $\mathrm{Re_p}$ and $\mathrm{M_p}$ for different wedge configurations are similar to the ones observed in Fig. 13.

6. Conclusions

To predict particle trajectories in complex hypersonic flows, drag coefficients needs to be accurately modeled over a wide range of Mach number, Reynolds number, and Knudsen number. Since no single empirical model is able to reproduce the drag coefficient behavior over these diverse regimes, a blended model was constructed. The new model combines the best performing empirical model for different combinations of regime. Experimental data that envelops a wide range of Re, M, and Kn was selected for comparison, and the model agrees within a standard deviation and a maximum error of 2.84% and 11.87%, respectively.

The blended model was then inserted into a Lagrangian particle trajectory model, and validations were performed for particle velocity and trajectory. The comparisons for ten different experimental test-cases were in excellent agreement, with results well within the uncertainties of the experiments. These results provide confidence that a Lagrangian particle trajectory model, equipped with the blended drag coefficient model, can accurately predict particle dynamics. Moreover, the approach is numerically efficient, allowing it to be used to predict the particle dynamics for particle-laden flows, at least for cases where inter-particle

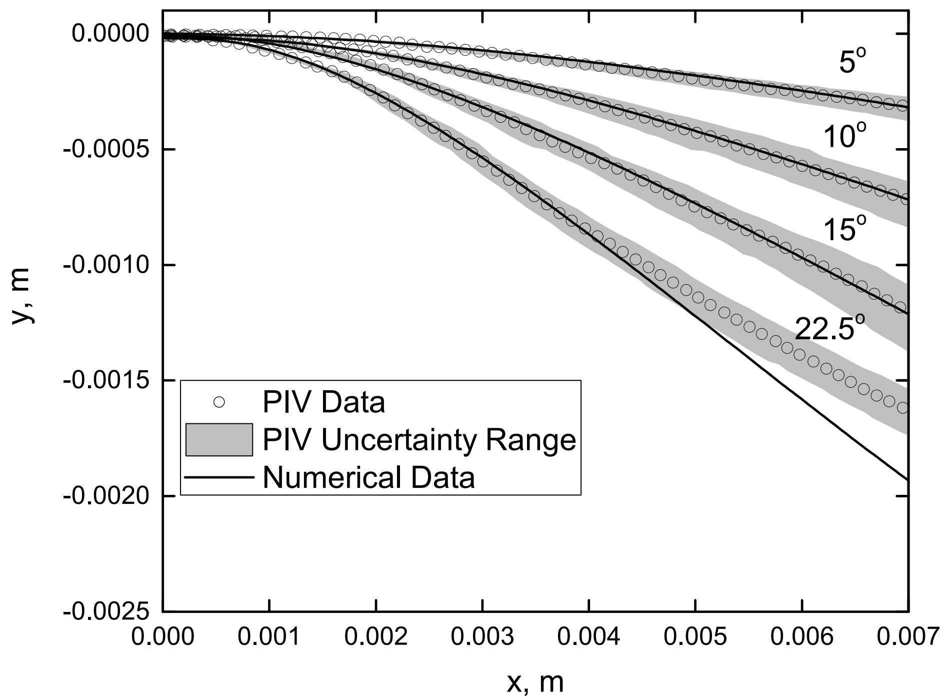

(a) Case - 1

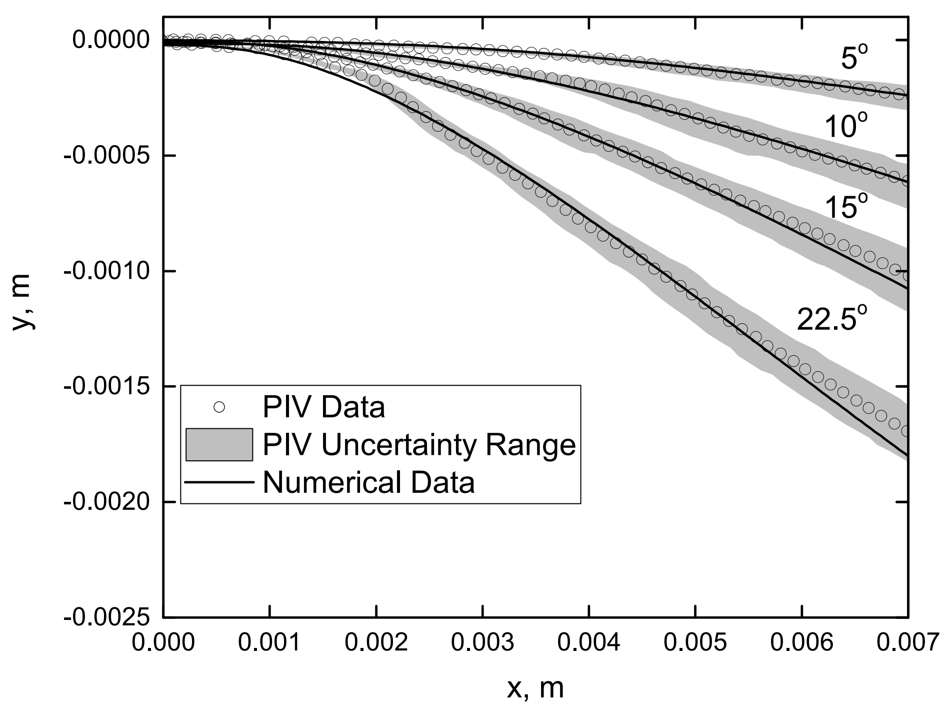

(b) Case - 2

Figure 16: Comparison of simulated trajectories with the ones retrieved from PIV data

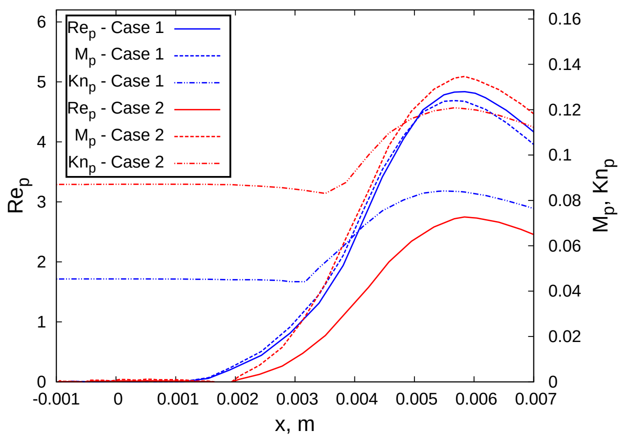

(a) 5° half angle wedge

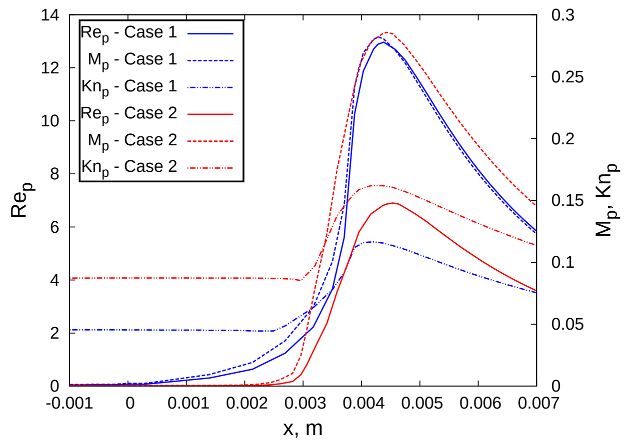

(b) 10° half angle wedge

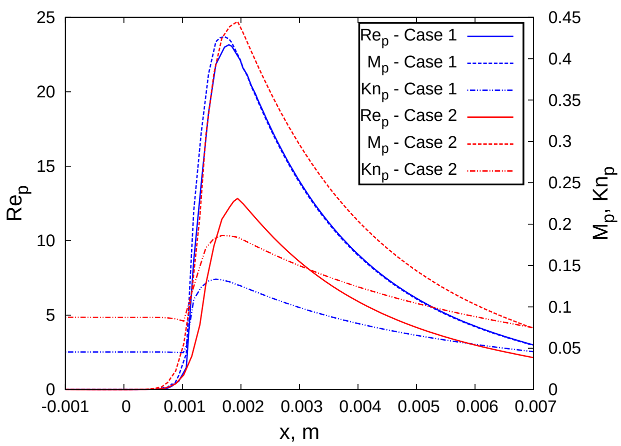

(c) 15° half angle wedge

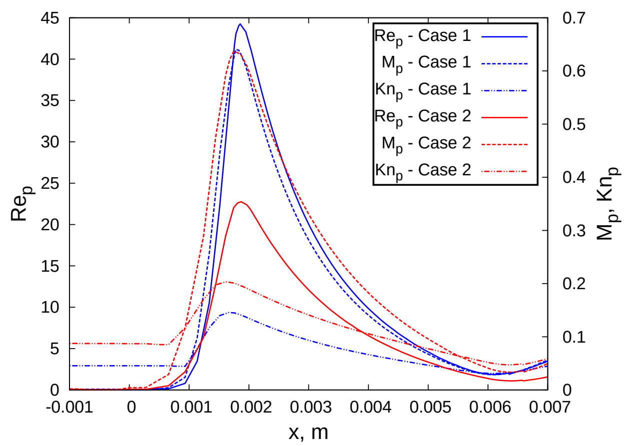

(d) 22.5° half angle wedge

Figure 17: Variation of Reynolds number, Mach number, and Knudsen number of particles travelling through flow fields for different half-angle wedge configurations and for two test conditions

interactions and structural deformations can be neglected.

The new blended model allows to predict the interactions of the particles with the flow field in situations where those capabilities are needed, such as the dust around an atmospheric entry capsule, the spalled particles of an ablating heat shield, or the metal oxide particulate inside a solid rocket plume.

Acknowledgements

Financial support for this work was provided by NASA Kentucky EPSCoR Award NNX10AV39A and NASA Award NNX13AN04A. The authors acknowledge G. Tedeschi for providing access to his thesis. The first author would also like to thank A. D. Ahmad, U. Düzel, and S. Schmitt for their assistance, as well as the librarians in charge of the InterLibrary Loan (ILL) at the University of Kentucky for going out of their way to provide the necessary material.

References

[1] C. J. Hwang, G. C. Chang, Numerical study of gas-particle flow in a solid rocket nozzle, AIAA Journal 26 (1988) 682–689. doi:10.2514/3.9953.

[2] W. S. Bailey, E. N. Nilson, R. A. Serra, T. F. Zupnik, Gas particle flow in an axisymmetric nozzle, ARS Journal 31 (1961) 793–798. doi:10.2514/8.5636.

[3] C. Henry, J.-P. Minier, Progress in particle resuspension from rough surfaces by turbulent flows, Progress in Energy and Combustion Science 45 (2014) 1–53. doi:10.1016/j.pecs.2014.06.001.

[4] P. Papadopoulos, M. E. Tauber, I.-D. Chang, Heatshield erosion in a dusty martian atmosphere, Journal of Spacecraft and Rockets 30 (1993) 140–151. doi:10.2514/3.11522.

[5] G. E. Palmer, Y. K. Chen, P. Papadopoulos, M. E. Tauber, Reassessment of effect of dust erosion on heatshield of mars entry vehicle, Journal of Spacecraft and Rockets 37 (2000) 747–752. doi:10.2514/2.3646.

[6] A. H. Lefebvre, V. G. MacDonell, Atomization and Sprays, second ed., CRC Press, Boca Raton, Florida, 2017. doi:10.1201/9781315120911.

[7] C. S. Campbell, Rapid granular flows, Annual Review of Fluid Mechanics 22 (1990) 57–90. doi:10.1146/annurev.fl.22.010190.000421.

[8] M. K. Langroudi, S. Turek, A. Ouazzi, G. I. Tardos, An investigation of frictional and collisional powder flows using a unified constitutive equation, Powder Technology 197 (2010) 91–101. doi:10.1016/j.powtec.2009.09.001.

[9] R. G. Gillies, C. A. Shook, J. Xu, Modelling heterogeneous slurry flows at high velocities, The Canadian Journal of Chemical Engineering 82 (2008) 1060–1065. doi:10.1002/cjce.5450820523.

[10] L. M. Lourenco, A. Krothapalli, On the accuracy of velocity and vorticity measurements with PIV, Experiments in Fluids 18 (1995) 421–428. doi:10.1007/BF00208464.

[11] L. M. Lourenco, A. Krothapalli, C. A. Smith, Particle image velocimetry, in: M. G. el Hak (Ed.), Advances in Fluid Mechanics Measurements, Springer-Verlag Berlin, Heidelberg, Germany, 1989, pp. 127–199. doi:10.1007/978-3-642-83787-6_4.

[12] T. Dracos (Ed.), Three-Dimensional Velocity and Vorticity Measuring and Image Analysis Technique: Lecture Notes from the short course held in Zurich, Switzerland, volume 4, Springer Science & Business Media, 1996. doi:10.1007/978-94-015-8727-3.

[13] Y. Yeh, H. Z. Cummins, Localized fluid flow measurements with an He-Ne laser spectrometer, Applied Physics Letters 4 (1964) 176–178. doi:10.1063/1.1753925.

[14] R. J. Adrian, R. J. Goldstein, Analysis of a laser doppler anemometer, Journal of Physics E: Scientific Instruments 4 (1971) 505–511. doi:10.1088/0022-3735/4/7/006.

[15] C. S. Peskin, The immersed boundary method, Acta Numerica 11 (2002) 479–517. doi:10.1017/S0962492902000077.

[16] V. Pasquariello, G. Hammerl, F. Orley, S. Hickel, C. Danowski, A. Popp, W. A. Wall, N. A. Adams, A cut-cell finite volume - finite element coupling approach for fluid-structure interaction in compressible flow, Journal of Computational Physics 307 (2016) 670–695. doi:10.1016/j.jcp.2015.12.013.

[17] B. E. Griffith, N. A. Patankar, Immersed methods for fluid-structure interaction, Annual Review of Fluid Mechanics 52 (2020) 421–448. doi:10.1146/annurev-fluid-010719-060228.

[18] M. Souli, D. J. Benson (Eds.), Arbitrary Lagrangian Eulerian and fluid-structure interaction: numerical simulation, ISBN 978-1-11-855788-4, John Wiley & Sons, Inc., Hoboken, New Jersey, 2013. doi:10.1002/9781118557884.

[19] J. H. Lundell, R. R. Dickey, The response of heat-shield materials to intense laser radiation, in: AIAA 16th Aerospace Sciences Meeting, AIAA Paper 1978-138, Huntsville, Alabama, 1978. doi:10.2514/6.1978-138.

[20] C. Park, J. H. Lundell, M. J. Green, W. Winovich, M. A. Covington, Ablation of carbonaceous materials in a hydrogen-helium arc-jet flow, in: AIAA 18th Thermophysics Conference, AIAA Paper 1983-1561, Montreal, Canada, 1983. doi:10.2514/3.48589.

[21] C. Park, Stagnation-point ablation of carbonaceous flat disks–Part I: Theory, AIAA Journal 21 (1983) 1588–1594. doi:10.2514/3.8293.

[22] C. Park, Stagnation-point ablation of carbonaceous flat disks–Part II: Experiment, AIAA Journal 21 (1983) 1748–1754. doi:10.2514/3.8319.

[23] C. Park, A. Balakrishnan, Ablation of galileo probe heat-shield models in a ballistic range, AIAA Journal 23 (1985) 301–308. doi:10.2514/3.8910.

[24] A. Martin, S. C. C. Bailey, F. Panerai, R. S. C. Davuluri, H. Zhang, A. R. Vazsonyi, Z. S. Lippay, N. N. Mansour, J. A. Inman, B. F. Bathel, S. C. Splinter, P. M. Danehy, Numerical and experimental analysis of spallation phenomena, CEAS Space Journal 8 (2016) 229–236. doi:10.1007/s12567-016-0118-4.

[25] S. C. C. Bailey, D. Bauer, F. Panerai, S. C. Splinter, P. M. Danehy, J. M. Hardy, A. Martin, Experimental analysis of spallation particle trajectories in an arc-jet environment, Experimental Thermal and Fluid Science 93 (2018) 319–325. doi:10.1016/j.expthermflusci.2018.01.005.

[26] R. S. C. Davuluri, H. Zhang, A. Martin, Effects of spalled particles thermal degradation on a hypersonic flow field environment, in: 54th AIAA Aerospace Sciences Meeting, AIAA Paper 2016-0248, San Diego, California, 2016. doi:10.2514/6.2016-0248.

[27] R. S. C. Davuluri, H. Zhang, A. Martin, Numerical study of spallation phenomenon in an arc-jet environment, Journal of Thermophysics and Heat Transfer 30 (2016) 32–41. doi:10.2514/1.T4586.

[28] R. S. C. Davuluri, Modeling of spallation phenomenon in an arc-jet environment, Master's thesis, University of Kentucky, Lexington, Kentucky, 2015. doi:10.13023/etd.2015.001.

[29] C. J. Roy, T. M. Smith, C. C. Ober, Verification of a compressible CFD code using the method of manufactured solutions, in: 32nd AIAA Fluid Dynamics Conference and Exhibit, AIAA Paper 2002-3110, St. Louis, Missouri, 2002. doi:10.2514/6.2002-3110.

[30] H. Weng, A. Martin, Multidimensional modeling of pyrolysis gas transport inside charring ablative materials, Journal of Thermophysics and Heat Transfer 28 (2014) 583–597. doi:10.2514/1.T4434.

[31] H. Zhang, H. Weng, A. Martin, Simulation of flow-tube oxidation on the carbon preform of PICA, in: 52nd AIAA Aerospace Sciences Meeting, AIAA Paper 2014-1209, National Harbor, Maryland, 2014. doi:10.2514/6.2014-1209.

[32] R. Fu, H. Weng, J. F. Wenk, A. Martin, Thermomechanical coupling for charring ablators, Journal of Thermophysics and Heat Transfer 32 (2018) 369–379. doi:10.2514/1.T5194.

[33] Ümran Düzel, O. M. Schroeder, H. Zhang, A. Martin, Computational prediction of NASA Langley HYMETS arc jet flow with KATS, in: 2018 AIAA Aerospace Sciences Meeting, AIAA Paper 2018-1719, Kissimmee, Florida, 2018. doi:10.2514/6.2018-1719.

[34] S. Balay, W. D. Gropp, L. C. McInnes, B. F. Smith, Efficient management of parallelism in object oriented numerical software libraries, in: E. Arge, A. M. Bruaset, H. P. Langtangen (Eds.), Modern Software Tools in Scientific Computing, Birkhäuser Press, Boston, MA, 1997, pp. 163–202. doi:10.1007/978-1-4612-1986-6_8.

[35] S. Balay, J. Brown, K. Buschelman, V. Eijkhout, W. D. Gropp, D. Kaushik, M. G. Knepley, L. C. McInnes, B. F. Smith, H. Zhang, PETSc Users Manual, Technical Report ANL-95/11 - Revision 3.3, Argonne National Laboratory, 2012.

[36] S. Balay, S. Abhyankar, M. F. Adams, J. Brown, P. Brune, K. Buschelman, V. Eijkhout, W. D. Gropp, D. Kaushik, M. G. Knepley, L. C. McInnes, K. Rupp, B. F. Smith, H. Zhang, PETSc Web page, http://www.mcs.anl.gov/petsc, 2014. URL: `http://www.mcs.anl.gov/petsc`.

[37] G. Karypis, V. Kumar, A fast and high quality multilevel scheme for partitioning irregular graphs, SIAM Journal on Scientific Computing 20 (1998) 359–392. doi:10.1137/S1064827595287997.

[38] D. W. Walker, J. J. Dongarra, Mpi: a standard message passing interface, Supercomputer 12 (1996) 56–58.

[39] H. Zhang, High Temperature Flow Solver for Aerothermodynamics Problems, Ph.d. thesis, University of Kentucky, Lexington, Kentucky, 2015. doi:10.13023/etd.2015.002.

[40] C. Crowe, J. D. Schwarzkopf, M. Sommerfeld, Y. Tsuji, Multiphase Flows with Droplets and Particles, ISBN 978-0-42-910639-2, second ed., CRC Press, Boca Raton, Florida, 2011. doi:10.1201/b11103.

[41] C. E. Brennen, Fundamentals of Multiphase Flows, ISBN 978-0-51-180716-9, Cambridge University Press, 2014. doi:10.1017/CBO9780511807169.

[42] G. Johnson, M. Massoudi, K. R. Rajagopal, A review of interaction mechanisms in fluid-solid flows, Technical Report DOE/PETC/TR-90/9, U. S. Department of Energy Pittsburg Energy Technology Center, Pittsburg, Pennsylvania, 1990. doi:10.2172/6443951.

[43] L. J. Forney, A. E. Walker, W. K. McGregor, Dynamics of particle-shock interactions: Part II: Effect of the basset term, Aerosol Science and Technology 6 (2007) 143–152. doi:10.1080/02786828708959127.

[44] S. L. Soo, Particulates and Continuum: Multiphase Fluid Dynamics, first ed., CRC Press, New York, 1989. doi:10.1201/9780203744291.

[45] P. J. Thomas, Experimentelle und theoretische Untersuchungen zum Folgeverhalten von Teilchen unter dem Einfluss grosser Geschwindigkeitsgradienten in kompressibler Strömung, Ph.d. thesis, Georg-August-Universität, Göttingen, Germany, 1991.

[46] G. Tedeschi, Etude théorique et expérimentale du comportement de particules à la traversée d'une discontinuité de vitesse (onde de choc), Ph.d. thesis, University of Aix-Marseille II, France, 1993.

[47] G. Tedeschi, M. Elena, H. Gouin, Particle motion through an oblique shock wave, in: Fifth International Conference on Laser Anemometry: Advances and Applications, volume 2052, International Society for Optics and Photonics, 1993, pp. 273–279. doi:10.1117/12.150514.

[48] R. R. Hughes, E. R. Gilliland, The mechanics of drops, Chemical Engineering Progress 48 (1952) 497–504.

[49] G. Bagheri, C. Bonadonna, On the drag of freely falling non-spherical particles, Powder Technology 301 (2016) 526–544. doi:10.1016/j.powtec.2016.06.015.

[50] N. A. Zarin, Measurement of non-continuum and turbulence effects on subsonic sphere drag, Contractor Report NASA-CR-1585, NASA, Washington, D.C., 1970. doi:2060/19700022558.

[51] A. B. Bailey, J. Hiatt, Sphere drag coefficient for a broad range of Mach and Reynolds numbers, AIAA Journal 10 (1972) 1436–1440. doi:10.2514/3.50387.

[52] C. T. Crowe, W. R. Babcock, P. G. Willoughby, Drag coefficient for particles in rarefied, low Mach-number flows, in: Proceedings of the International Symposium on Two-Phase Systems, Pergamon Press, 1972, pp. 419–431. doi:10.1016/B978-0-08-017035-0.50027-6.

[53] A. B. Bailey, Sphere drag coefficient for subsonic speeds in continuum and free-molecule flows, Journal of Fluid Mechanics 65 (1974) 401–410. doi:10.1017/S0022112074001443.

[54] E. Loth, Compressibility and rarefaction effects on drag of a spherical particle, AIAA Journal 46 (2008) 2219–2228. doi:10.2514/1.28943.

[55] S. A. Schaaf, P. L. Chambre, Flow of rarefied gases, in: C. duP. Donaldson (Ed.), Princeton Aeronautical Paperbacks, 8, Princeton University Press, Princeton, New Jersey, 1961.

[56] H.-S. Tsien, Superaerodynamics, mechanics of rarefied gases, Journal of Aeronautical Sciences 13 (1946) 653–664. doi:10.2514/8.11476.

[57] M. N. Macrossan, Scaling parameters for hypersonic flow: correlation of sphere drag data, in: M. S. Ivanov, A. K. Rebrov (Eds.), 25th International Symposium on Rarefied Gas Dynamics, volume 1, Siberian Branch of the Russian Academy of Sciences, St. Petersburg, Russia, 2007, pp. 759–764.

[58] J. Aroesty, Sphere drag in a low density supersonic flow, Technical Report HE-150-192, Institute of Engineering Research, University of California, Berkeley, California, 1962. doi:2060/19630011721.

[59] W. D. Hayes, R. F. Probstein, Hypersonic Flow Theory, Academic Press, New York, 1959.

[60] R. T. Davis, I. Flügge-Lotz, Second-order boundary-layer effects in hypersonic flow past axisymmetric blunt bodies, Journal of Fluid Mechanics 20 (1964) 593–623. doi:10.1017/S0022112064001422.

[61] A. B. Bailey, J. Hiatt, Free-flight measurements of sphere drag at subsonic, transonic, supersonic, and hypersonic speeds for continuum, transition, and near-free-molecular flow conditions, Technical Report AEDC-TR-70-291, Arnold Engineering Development Center, Arnold Air Force Station, Tennessee, 1971. doi:100.2/AD0721208.

[62] S. F. Hoerner, Fluid-Dynamic Drag, Bakkersfield, California, 1965.

[63] J. V. Sengers, Y. Y. L. Wang, B. Kamgar-Parsi, J. R. Dorfman, Kinetic theory of drag on objects in nearly free molecular flow, Physica A: Statistical Mechanics and its Applications 413 (2014) 409–425. doi:10.1016/j.physa.2014.06.026.

[64] N. A. Zarin, J. A. Nicholls, Sphere drag in solid rockets - non-continuum and turbulence effects, Combustion Science and Technology 3 (1971) 273–285. doi:10.1080/00102207108952295.

[65] C. W. Oseen, Über die stoke'sche formel und über eine verwandte aufgabe in der hydrodynamik, Arkiv för Matematik Astronomi och Fysik 6 (1911).

[66] L. Schiller, Z. Naumann, A drag coefficient correlation, VDI Zeitung 77 (1935) 318–320.

[67] L. B. Torobin, W. H. Gauvin, Fundamental aspects of solids-gas flow: Part I: Introductory concepts and idealised sphere motion in viscous regime, The Canadian Journal of Chemical Engineering 37 (1959) 129–141. doi:10.1002/cjce.5450370401.

[68] M. J. Walsh, Drag coefficient equations for small particles in high speed flows, AIAA Journal 13 (1975) 1526–1528. doi:10.2514/3.7026.

[69] E. Cunningham, On the velocity of steady fall of spherical particles through fluid medium, in: Proceedings of the Royal Society of London, volume 83 of *Series A, Containing Papers of a Mathematical and Physical Character*, Royal Society, 1910, pp. 357–365. doi:10.1098/rspa.1910.0024.

[70] G. Tedeschi, H. Gouin, M. Elena, Motion of tracer particles in supersonic flows, Experiments in Fluids 26 (1999) 288–296. doi:10.1007/s003480050291.

[71] D. J. Carlson, R. F. Hoglund, Particle drag and heat transfer in rocket nozzles, AIAA Journal 2 (1964) 1980–1984. doi:10.2514/3.2714.

[72] C. B. Henderson, Drag coefficients of spheres in continuum and rarefied flows, AIAA Journal 14 (1976) 707–708. doi:10.2514/3.61409.

[73] R. A. Millikan, The general law of fall of a small spherical body through a gas, and its bearing upon the nature of molecular reflection from surfaces, Physical Review 22 (1923) 1–23. doi:10.1103/PhysRev.22.1.

[74] R. J. Stalder, J. V. Zurick, Theoretical aerodynamic characteristics of bodies in a free-molecule-flow-field, NACA Technical Note NACA-TN-2423, National Advisory Committee for Aeronautics, Moffett Field, California, 1951. doi:2060/19930083019.

[75] P. Langevin, Une formule fondamentale de théorie cinétique, Annales de Chimie et de Physique 5 (1905) 245–288.

[76] P. S. Epstein, On the resistance experienced by spheres in their motion through gases, Physical Review 23 (1924) 710–733. doi:10.1103/PhysRev.23.710.

[77] W. R. Lawrence, Free-flight range measurements of sphere drag at low Reynolds numbers and low Mach numbers, Technical Report AEDC-TR-67-218, Arnold Engineering Development Center, Arnold Air Force Station, Tennessee, 1967. doi:100.2/AD0660545.

[78] E. D. Kane, Sphere drag data at supersonic speeds and low Reynolds numbers, Journal of the Aeronautical Sciences 18 (1951) 259–270. doi:10.2514/8.1924.

[79] P. P. Wegener, H. Ashkenas, Wind tunnel measurements of sphere drag at supersonic speeds and low Reynolds numbers, Journal of Fluid Mechanics 10 (1961) 550–560. doi:10.1017/S0022112061000354.

[80] A. K. Sreekanth, Drag measurements on circular cylinders and spheres in the transition regime at a Mach number of 2, UTIA Report 74, Institute of Aerophysics, University of Toronto, Ontario, Canada, 1961.

[81] F. S. Sherman, New Experiments on Impact-Pressure Interpretation in Supersonic and Subsonic Rarefied Air Streams, Technical Note 2995, National Advisory Committee for Aeronautics, Washington, 1953. doi:2060/19930083740.

[82] E. L. Clark, Aerodynamic characteristics of the hemisphere at supersonic and hypersonic Mach numbers, AIAA Journal 7 (1969) 1385–1386. doi:10.2514/3.5359.

[83] L. L. Kavanau, Base pressure studies in rarefied supersonic flows, Journal of the Aeronautical Sciences 23 (1956) 193–230. doi:10.2514/8.3536.

[84] H. H. Kurzweg, Interrelationship between boundary layer and base pressure, Journal of the Aeronautical Sciences 18 (1951) 743–748. doi:10.2514/8.2094.

[85] R. Lehnert, Base Pressure of Spheres at Supersonic Speeds, NavOrd Report 2774, U. S. Naval Ordnance Laboratory, White Oak, Maryland, 1953.

[86] S. Goldstein, Modern Developments in Fluid Dynamics: An Account of Theory and Experiment Relating to Boundary Layers, Turbulent Motion and Wakes, volume 1, Oxford at the Clarendon Press, London, 1938, pp. 492–529.

[87] P. J. Thomas, K. A. Butefisch, K. H. Sauerland, On the motion of particles in a fluid under the influence of a large velocity gradient, Experiments in Fluids 14 (1993) 42–48. doi:10.1007/BF00196986.

[88] C. B. Ross, L. M. Lourenco, A. Krothapalli, Particle image velocimetry measurements in a shock-containing supersonic flow, in: 32nd Aerospace Sciences Meeting and Exhibit, AIAA Paper 1994-0047, Reno, Nevada, 1994. doi:10.2514/6.1994-47.

[89] R. F. Hoglund, Recent advances in gas-particle nozzle flows, ARS Journal 32 (1962) 662–671. doi:10.2514/8.6121.

[90] W. D. Brennan, The effects of nozzle geometry on particle size distribution in a small two dimensional rocket motor, Ph.d. thesis, Naval Postgraduate School, Monterey, California, 1989. doi:10945/25882.

[91] C. B. Ross, Calibration of Particle Image Velocimetry in a Shock-Containing Supersonic Flow, Master's thesis, The Florida State University, Tallahassee, Florida, 1993.

[92] B. R. Maxwell, R. G. Seasholtz, Velocity lag of solid particles in oscillating gases and in gases passing through normal shock waves, Technical Note NASA TN D-7490, NASA, Cleveland, Ohio, 1974. doi:2060/19740010805.